

FOR NUCLEAR RESEARCH

CERN/DRDC 91-18
DRDC/P28
22 March, 1991



**PROPOSAL to the DRDC**

# R & D FOR COLLIDER BEAUTY PHYSICS AT THE LHC

J. Ellett, S. Erhan, D. Lynn, M. Medinnis, P. Schlein*), J. Zweizig
University of California, Los Angeles, CA, U.S.A.

G. Engelmann, O. Klingsheim, Hartmut Wahl
CERN, Geneva, Switzerland

A. Czermak
Institute of Nuclear Physics, Cracow, Poland

W. Hofmann, K.T. Knöpfle
Max-Planck Institute fur Kernphysik, Heidelberg, F.R.G.

C. Joseph, J.P. Perroud, M.T. Tran
University of Lausanne, Lausanne, Switzerland.

E. Hartouni, M. Kreisler
University of Massachusetts, Amherst, MA, U.S.A.

B. Knapp
Nevis Laboratory, Columbia University, Irvington-on-Hudson, NY, U.S.A.

R. Dzhelyadin, Y. Guz, V. Kubic, V. Obraztsov, A. Ostankov
IHEP-Serpukhov, Protvino, U.S.S.R.

R. Harr, P. Karchin, C. Liapis, J. Sinnott
Yale University, New Haven, CT, U.S.A.

P. Bogunovic, G. Paic, D. Rendic, D. Vranic
Rudjer Boskovic Institute[1], Zagreb, Croatia, Yugoslavia

**Abstract:** We propose an R&D program for the development of a Beauty trigger and innovative elements of the associated spectrometer. A series of short test runs is proposed at the $S\bar{p}pS$ Collider with the minimal spectrometer which will allow a credible B signal to be obtained in an invariant mass spectrum of reconstructed B mesons. The program builds on the success of the recent $S\bar{p}pS$ collider run of the P238 Collaboration, in which clean signals from beam-beam interactions were observed in a large silicon strip microvertex detector running 1.5 mm from the circulating beams. A continuing successful R&D program of the type proposed could ultimately lead to a collider experiment at the LHC to study CP-Violation and rare B decays.

---

*) Spokesman

[1] Pending approval of the Institute.

## TABLE OF CONTENTS



---

# *1. OVERVIEW*

One of the most challenging and important problems at the Large Hadron Collider will be how to best study the rare decays of Beauty particles as a probe of possible new physics beyond the Standard Model and of the source of CP-Violation. The several hundred $\mu$barn cross section for $B\bar{B}$ production expected at the LHC, coupled with sophisticated trigger processor techniques, should make possible the necessary acquisition of enormous samples of exclusive Beauty decays.

Between 1988 and 1990 our predecessor collaboration,[1] P238, undertook a major effort to understand how to use Hadron Colliders as B-Factories. A proposal was presented to the SPS-Committee for a new detector to study Beauty physics at the SPS-Collider. New triggering ideas were proposed, in which all information is derived from real time processing of data from the silicon microvertex detector.

The Research Board approved P238 to install and run a large silicon strip microvertex detector inside the vacuum pipe of the LSS5 Interaction Region during the 3-month run from September-December 1990, noting that: **"the technique to be developed as part of the proposed test was quite relevant to the instrumentation needed for the LHC environment"**. With the silicon detectors positioned 1.5 mm from the circulating beams, clean signals from beam-beam interactions were observed with no evidence of either RF pickup from the circulating beams or significant background from beam halo.

APPENDIX C contains a DRAFT of a paper to be submitted to NIM, entitled: **"Development and Test of a Large Silicon Strip System for a Hadron Collider Beauty Trigger"**, which summarizes the P238 silicon detector effort and presents some of the data analysis results. **These results satisfy the major concern about using a hadron collider as a triggerable "B-Factory", namely whether background**

---

[1] Proposal P238, Study of Beauty Physics at the SPS-Collider with Real-Time Use of Silicon Microvertex Information, CERN-SPSC/88-33;
P238Add.1, Measurement of $B_s$ Mixing, CERN-SPSC/89-43;
P238Add.2, Request For Collider Test of Silicon Microvertex Detector, CERN-SPSC/89-55;
P238Add.3, Further Comments on Collider Test of Silicon Microvertex Detector, CERN-SPSC/89-61.

**and/or RF pickup would prohibit running a silicon microvertex detector in close proximity to the circulating beams.**

The R&D program proposed in the present document builds on these successes. Since a hadron collider Beauty experiment with efficient triggering and particle identification has never existed, and many of the technological problems of triggering are indeed new and formidable, the next major step must be to complete the trigger, by interfacing the silicon readout to an appropriate processor system, and demonstrate its efficiency by actually using it to trigger a relatively inexpensive prototype spectrometer. The processor must be capable of performing, in real time, the calculations which allow a sufficiently intelligent trigger decision to be made.

Both detector R&D and continued collider test runs are required in order to demonstrate the effectiveness and reliability of the proposed trigger. **The primary end goal of our proposed R&D effort is to observe a credible Beauty signal in a proposed 1993 run with $\int \mathcal{L} dt = 0.5\ pb^{-1}$ at the $S\bar{p}pS$-Collider.** A proposed short collider run in 1992 will be used to test a Data-Driven-Processor interfaced to the same silicon system used in the 1990 run. In addition, we will test the detector technology which is crucial for operation at the LHC[2] with luminosity $\mathcal{L} > 10^{31}$.

In Chapter 2, we discuss the proposed R&D program and its various "milestones". Chapter 3 contains an estimate of the expected Beauty event yield using a prototype spectrometer with 400 mrad aperture. We find that credible B signals could be obtained in an $S\bar{p}pS$-Collider run with $\int \mathcal{L} dt = 0.5\ pb^{-1}$. Chapter 4 contains a description of the prototype spectrometer elements and defines their necessary properties. In Chapter 5, we discuss the required resources and their costs.

There are three APPENDICES. A contains a description of the Level-1 trigger algorithm and its implementation in a Data-Driven Processor. B describes details of the silicon readout system and interface to the data driven processor. C contains the draft NIM article on the 1990 silicon test run refered to above.

We note that the advanced R&D project on Fast RICH detectors of J. Seguinot & T. Ypsilantis (supported by IN2P3, PSI and CERN-LAA) is of great interest to us and we are collaborating on the use of such detectors in the prototype spectrometer discussed in Chapter 4 of this document. Indeed, many of the results of their program are contained in Section 4.6. We also mention that parallel DRDC proposals by Weilhammer et al. (Silicon detector development) and Ypsilantis et al. (Liquid Xenon/Krypton Calorimetry) deal with detector topics that are of essential interest to us in an eventual LHC experiment on Beauty physics and we are also in close contact with those groups.

Finally, in order to clarify the context in which we propose this R&D program, Table 1 compares the essential characteristics which determine the Beauty yield of the prototype R&D device proposed in this document with possible full experiments at the $S\bar{p}pS$ and LHC and at a potential $e^+e^-$-collider B-Factory. If our R&D program succeeds in demonstrating the expected efficient triggering and reconstruction of Beauty particles, the conclusions to be drawn from Table 1 are:

- A program of Beauty physics could be carried out at the $S\bar{p}pS$-Collider which is at least as good as that expected from the $e^+e^-$-Collider B-Factory.
- An additional two orders-of-magnitude in statistics will likely be available in a dedicated collider Beauty experiment at the LHC.

---

[2] Erhan et al., **Collider Beauty Physics at LHC**, CERN/PPE 91-10, Proceedings of Workshop on LHC Physics, Aachen, FRG (4-9 Oct., 1990).

*Table 1: Rate Comparison[a] of Proposed R&D Device with Other Options.*

| | This R&D Proposal | Full Exp. $S\bar{p}pS$ | Full Exp. LHC | $e^+e^-$ B-Factory |
|---|---|---|---|---|
| $\sigma(b\bar{b})$ | $15 \cdot 10^{-30}$ | $15 \cdot 10^{-30}$ | $300 \cdot 10^{-30}$ | $10^{-33}$ |
| $\mathcal{L}^b$ | $6 \cdot 10^{29}$ | $5 \cdot 10^{30}$ | $10^{31}$ | $3 \cdot 10^{33}$ |
| Acceptance[c] | 6% | 20% | 50% | 80% |
| $\sigma \cdot \mathcal{L} \cdot A$ | 0.5 Hz | 15 Hz | 1500 Hz | 2 Hz |

(a) These rates are for a fictitious final state with unit branching ratio and trigger efficiency. Calculations for the P238 proposal indicate that trigger efficiencies larger than 30% are to be expected in the hadron collider experiments. Other efficiencies are expected to be comparable in hadron and electron colider Beauty experiments.

(b) The relatively low luminosity for this R&D proposal assumes 3-bunch operation.

(c) The geometric acceptances for the complete $S\bar{p}pS$ and LHC experiments correspond to spectrometers with 600 mrad aperture on both outgoing arms.

## *2. PROPOSED R&D PROGRAM & MILESTONES*

We outline here the proposed program for the years 1990-1994. Of course, 1990 is behind us, but the accomplishments of the P238 $S\bar{p}pS$-Collider run provide the "driving force" and the basis of the entire proposed program. We have learned how to build and operate a type of silicon microvertex system that could be the basis of a Beauty trigger at the $S\bar{p}pS$-Collider and presumably also at other existing and future hadron colliders. The demonstration that such a system sees tracks from interactions with essentially no background implies that sufficiently powerful real-time calculations on the silicon data should make possible the necessary suppression of minimum bias background, while retaining a sufficiently large fraction of the desired beauty events.

Very extensive Monte-Carlo simulation calculations were performed to develop an appropriate trigger algorithm for the P238 proposal. Such calculations were also carried out by Erhan et al. for the LHC Aachen workshop (see CERN/PPE 91-10). The steps of this algorithm are summarized in APPENDIX A as part of a discussion of the Data-Driven Level-1 Trigger Processor, which is currently under construction. We anticipate having a running processor with a VME data acquisition system (see APPENDIX B) by fall 1991. Testing in 1991 will be done off line with Monte-Carlo data and with the $10^7$ minimum bias events which were written to tape during the 1990 silicon run.

APPENDIX B also contains a description of a new silicon detector readout with processor interface. The principle features of this system are to allow full parallel readout of all silicon detectors with flexible sparse readout capability and local analog-to-digital converters at the detectors.

**1992 Collider Run:** We propose to test the Data-Driven-Processor interfaced to the existing P238 silicon system in LSS5 during a 3-week collider run in Fall 1992 (not counting "critical days"), in order to obtain a large sample of real beauty and charm events. It will be a natural "sequel" to the P238 1990 silicon run and should yield a large enough data sample to allow topological identification of some Beauty events (e.g. those with tertiary vertices). Such a data-taking run at the collider would also guarantee success in the 1993 run, when we use the system to trigger a prototype spectrometer. We also request a one-month parasitic fixed target test beam run in the North Hall H8 beam during 1992, in order to bring up and test the silicon-processor system before installation in LSS5.

**1993 Collider Run:** We propose a run in LSS5 with $\int \mathcal{L} dt = 0.5\ pb^{-1}$, in which we use the silicon-processor system to trigger the prototype spectrometer described in Chapter 4. Our primary goal is to demonstrate a clean reconstructed beauty signal with low background from all sources, including direct charm production. In order to achieve this goal, the spectrometer must be ready for September or October 1993 installation in LSS5. The major detector items are drift chambers, RICH counters and a new silicon $\mu$vertex detector. With early approval, we would have sufficient time to have these detectors in a fixed target test beam before the collider installation.

Additional R&D test runs at the $S\bar{p}pS$-Collider after 1993 may be useful and desirable. However, we do not comment on such options at the present time.

## 3. ESTIMATION OF BEAUTY EVENT YIELD

In order to estimate the expected Beauty event yield vs. spectrometer aperture, we consider the following B-decay final state with all charged particles, which has the largest known[3] branching fraction [$0.012 \times 0.55 \times 0.119 = 7.85 \times 10^{-4}$]. We also include in the following estimate, the expected observations of other exclusive final states.

$$\bar{B}^0 \rightarrow D^{*+}\pi^+\pi^-\pi^- \rightarrow (D^0\pi^+)\pi^+\pi^-\pi^-$$

$$D^0 \rightarrow K^-\pi^-\pi^+\pi^+ \ (7.8\%), \ K^-\pi^+ \ (3.7\%), \ K^-K^+ \ (0.4\%)$$

The calculated geometrical acceptance of this B decay sequence (with the $D \rightarrow K3\pi$ channel) is 6%, for a single-arm spectrometer with 400 mrad aperture (see Chapter 4). The Monte Carlo calculations are made at $\sqrt{s} = 630$ GeV using the PYTHIA event generator. Events are considered accepted if all decay tracks fall within the given aperture and have momentum larger than 200 MeV.

The event yield estimate depends on the following parameters (where we assume a run with integrated luminosity, $\int \mathcal{L} dt = 0.5$ pb$^{-1}$). The Trigger and Event Reconstruction Efficiencies are conservative values estimated in the original P238 proposal. The "Factor for Other Exclusive Final States" includes: $B^0 \rightarrow D^{*+}\pi^-$ (0.28%), $D^+\pi^-$ (0.48%), and $B^- \rightarrow D^0\pi^-$ (0.2%), $D^{*+}\pi^-\pi^-$ (0.26%). For $D^+$ decay, we use the final state $K^-\pi^+\pi^+$ with B.R. = 7.7%.

| | |
|---|---|
| $\sigma(b\bar{b})$ | $15 \times 10^{-30}$ |
| $\int \mathcal{L} dt$ | $5 \times 10^{35}$ (1/2 "inverse pbarn") |
| Probability( $b \rightarrow \bar{B}^0$ ) | 40% |
| Branching Fraction | $7.85 \times 10^{-4}$ |
| Geometrical Acceptance | 6% |
| Trigger Efficiency | 30% |
| Event Reconstruction Efficiency | 35% |
| Factor for ($b \rightarrow \bar{B}^0$ or $\bar{b} \rightarrow B^0$) | 2 |
| Factor for Other Exclusive Final States | 2.23 |
| RECONSTRUCTED EVENT YIELD | 61 EVENTS |

Fig. 1 from the P238 proposal, shows a Monte-Carlo simulation of the invariant mass distribution we expect for the $D^*3\pi$ final state. The expected combinatoric background is also included in the distribution. The cleanliness of the signal implies that it can be shown to exist with very few events.

In addition to the above exclusive final states with all charged particles, we expect about 450 semi-leptonic final states from $B^0$ decay with a reconstructed $D^*$. These have unique topologies, with the $D^*$ and a lepton (e or $\mu$) coming from a secondary vertex which is more than 0.5 mm downstream of the primary vertex (this is the vertex cut[4] which was found to be necessary in the analysis for the

[3] Argus Collaboration; Z. Physik C 48 (1990) 543.

[4] The losses due to this cut are included in the 35% event reconstruction efficiency used in the rate estimates. This efficiency as well as the trigger efficiency are the result of extensive Monte Carlo calculations carried out for the original P238 proposal.

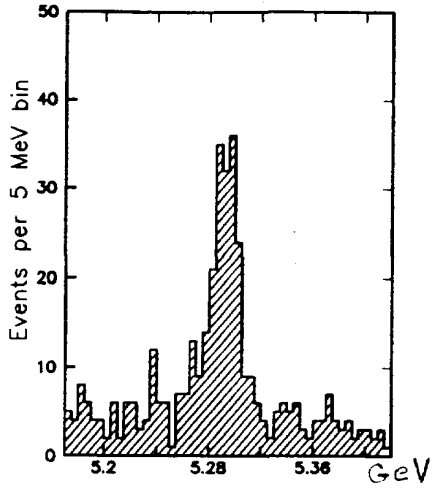


*Figure 1: Simulated $\bar{B}^0$-Meson Invariant Mass Distribution.* The expected $\bar{B}^0$ signal in the channel: $\bar{B}^0 \to D^{*+}\pi^+\pi^-\pi^-$, $D^{*+} \to D^0\pi^+$, $D^0 \to K^-\pi^-\pi^+\pi^+$, after all $D^{*+}$ and $D^0$ mass constraints, topology and transverse momentum balance cuts have been applied. The background shown is an estimate from all sources at the SpS-Collider.

P238 proposal). There will also be a substantial number of other partially reconstructed non-leptonic final states with a $D^*$ at a secondary vertex.

Fig. 2 shows the expected momentum distribution of accepted B-Meson events with a 400 mrad aperture. The mean momentum is about 45 GeV, which is somewhat larger than the value 35 GeV given in the P238 proposal for a 600 mrad spectrometer. The mean B decay distance will be about 3 mm and, as shown in the P238 proposal, will be measured with a resolution of about 6%. Fig. 3 shows the momentum distribution of the decay tracks from accepted $D^*3\pi$ events.

We have thus far not addressed the important question of background from direct $c\bar{c}$ (charm) production, which is expected at the SpS to have a cross section about two orders-of-magnitude larger than the $b\bar{b}$ cross section. A considerable effort was expended in the preparation of the original P238 proposal to understand this point. There were two important conclusions. First, due to the smaller average lifetime and final state multiplicities of charm decay compared to beauty decay, the trigger efficiency using our silicon microvertex detector is more than ten times smaller for charm. Second, it was found that, in offline reconstruction based on the use of secondary and tertiary vertices seen in the microvertex detector, the topological and large energy release differences between the two cases allow the rejection of charm background below the level of combinatoric background in beauty reconstruction. The final conclusion was that direct charm background was not a major concern. However, as was stated above in Chapter 2, one aspect of the goals in this R&D program is to demonstrate the correctness of this conclusion.

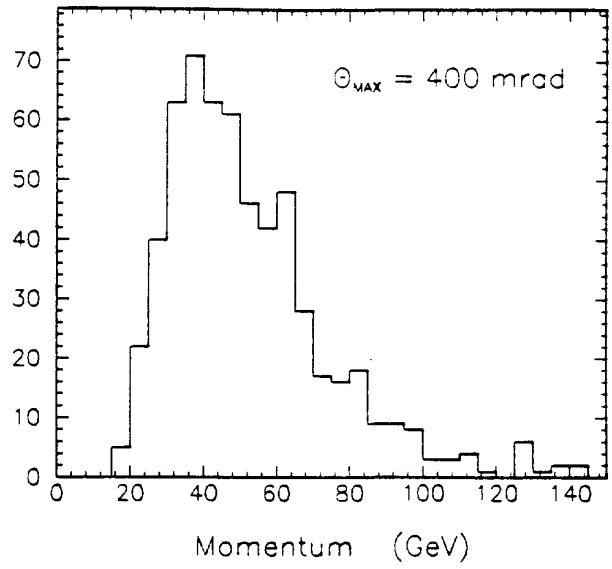


*Figure 2: Momentum of Accepted Beauty Mesons for a 400 Mrad Spectrometer.* The calculations are carried out for the $D^*3\pi$ final state discussed in the text.

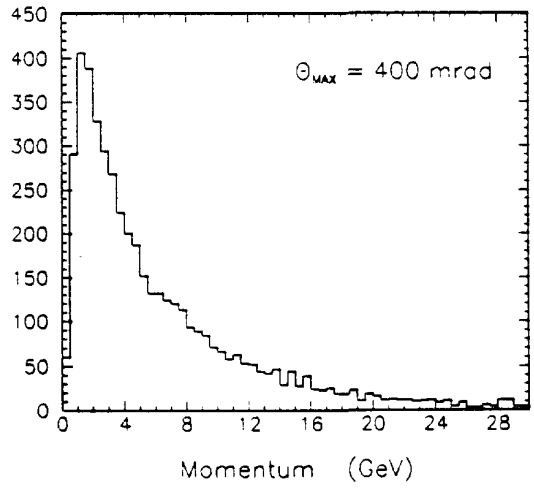


*Figure 3: Momentum of Beauty Meson Decay Tracks with a 400 mrad. Spectrometer.* The calculations are carried out for the $D^*3\pi$ final state discussed in the text.

## *4. SPECTROMETER ELEMENTS*

The proposed prototype spectrometer with aperture $10 < \theta < 400$ mrad is shown in Fig. 4. In this chapter, we give detailed descriptions of the following components:

- **Silicon-strip microvertex detector:** installed at the center of the interaction region inside the vacuum chamber. It matches the forward spectrometer system and therefore has a geometry typical of fixed-target experiments with its planes perpendicular to the circulating beams.

- **Vacuum Pipe:** contains the circulating beams and passes through the various detector components. It is made of two thin windows connected by a conical section.

- **Magnet:** has a field integral of 4.6 Tm and a circular aperture with diameter 160 cm. Beam orbit correction magnets are also required, because no septum plate is used to shield the circulating beams.

- **Pixel Detectors:** useful for matching x/y views and in connecting tracks found in the silicon detectors with those found in the wire chamber system. Silicon pixel detectors may be positioned just after the silicon strip detectors. A pixel drift chamber is positioned immediately after the first window.

- **Jet Drift Chambers:** positioned inside the upstream end of the magnet and just downstream of the magnet. Jet-type drift cells are used to measure the position and direction of charged tracks.

- **Ring Imaging CHerenkov (RICH) Counters:** Liquid and gas RICH counters are used for off-line particle identification.

### *4.1 Silicon-Strip Microvertex Detector*

**Geometry:** To match the forward spectrometer system, the silicon microvertex detector has a geometry typical of fixed-target experiments, with the silicon planes installed perpendicular to the circulating beams, inside the vacuum chamber. The extended source size of the bunch crossing region and the need to minimize the extrapolation distance from measured track points in the silicon to an interaction vertex leads to a detector design in which the silicon planes are distributed along the intersection region.[5] Each detector plane consists of four quadrant detectors mounted on rigid but movable supports such that, during beam manipulations, the upper and lower halves can be retracted to a safe position 5 cm or more from the beams.

The existing 6-plane silicon strip system which is described in the NIM draft article in APPENDIX C (see Figs. 1-6 in APPENDIX C), will be used for the 1992 run. Thus the existing Roman pot mechanism will be used. For the 1993 run, however, a new and larger silicon detector system will be constructed to provide more complete vertex acceptance. Calculations for the P238 proposal showed that 16 silicon planes spaced every 4 cm in the longitudinal direction yielded about 95% acceptance of the vertex distribution. Thus we plan to construct such a system. Detectors with double-sided readout will be used.

---

[5] The silicon detectors are positioned symmetrically with respect to the interaction region center, since the trigger algorithm (see APPENDIX A) uses tracks in both hemispheres.

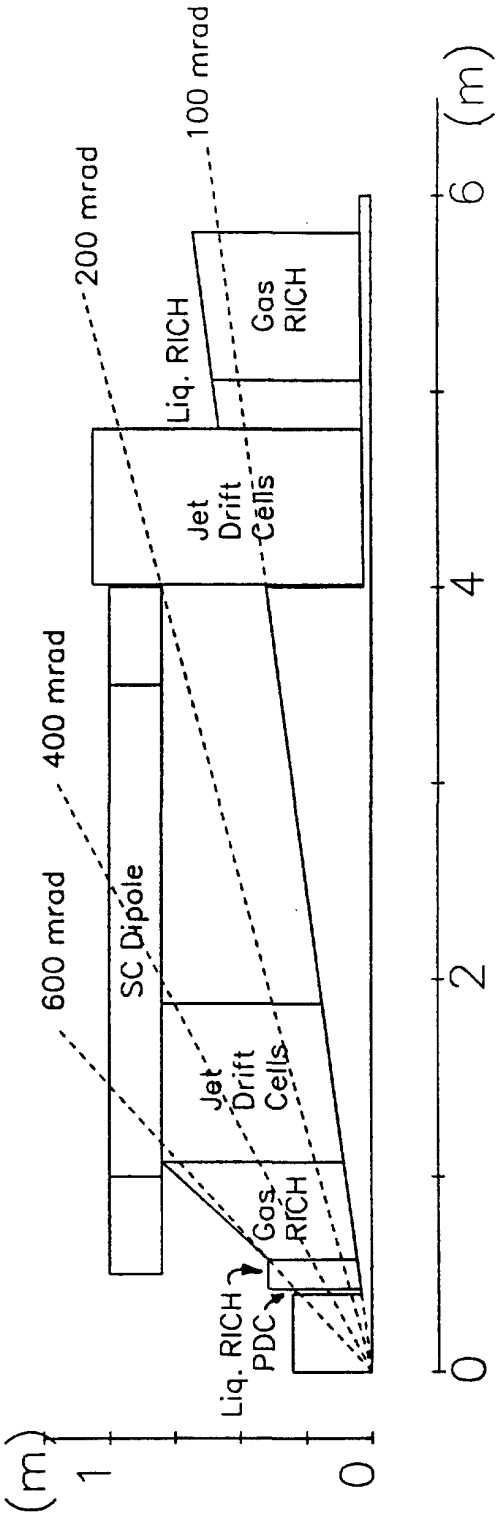


*Figure 4: Layout of Spectrometer.* The silicon strip and pixel detectors (not seen in sketch) are positioned at z = 0. After the vacuum windows at z = 40 and 400 cm, there are pixel drift chambers discussed in the text.

A new, larger Roman pot and associated positioning mechanism will have to be designed. Our experience with the P238 tests show that we can expect to run with a gap between upper and lower detector assemblies of less than 3 mm without significant background. Clearly this places great demands on the stability and precision of the support assembly, which will be patterned after the the existing Roman pot technology at CERN. We also note that new monitoring electronics for the low-beta quadrupole magnet currents will be necessary in order to dump the circulating beams in less than one turn should it be necessary for the protection of the silicon. Although, we experienced no problems during the 3-month 1990 run, precautions should be taken to protect the larger and more expensive silicon system planned for the 1993 run.

**Installation in Vacuum:** There are two major problems with using silicon inside the ultra-high vacuum of a collider very close to circulating beams:

1. RF pick-up in the silicon generated by passage of beam bunches,

2. The need to preserve an ultra-high vacuum in the beam pipe which imposes very tight restrictions on detector materials and requires tightly sealed feed-throughs on signal paths.

An effective solution to these problems, which was employed in the P238 silicon system, was to separate the silicon detectors from the machine vacuum with a thin aluminum "window", which approximately follows the contour of the detectors. The aluminum serves both as an RF shield and as a means of isolating the ultra-high vacuum of the machine from outgassing of detector materials and also relaxes the requirements on feed-through seals. Collapse of these thin windows is prevented by creating a secondary vacuum inside the Roman pots.

The silicon detectors are mounted inside a vessel, which is modeled after the CERN Roman pot. The thin aluminum window constitutes the bottom of the "pot" (see figures in APPENDIX C).

Because no significant RF pickup was observed in the P238 tests at the CERN $Sp\bar{p}S$-Collider, a thinner aluminum window will be used in the future, in order to minimize multiple scattering. The criterion is that it be thin compared to a single 250 $\mu$m thick silicon detector, while still providing adequate RF shielding. A 100 $\mu$m aluminum shield should be a reasonable compromise. This will be tested during the 1992 collider run.

**Silicon-Strip Detectors with Readout on Both Sides:** To optimize the selectivity of the silicon microvertex detector, it will be essential to combine optimal spatial resolution with very little material in the sensitive area. This can be achieved by using both sides of the silicon wafer to extract spatial information. Such detectors, where strips on both sides are read out, have been developed by several groups. A CERN group has developed ac-coupled double-sided detectors,[6] using a novel scheme to separate strips resistively on the n-side by means of field depletion via a suitable potential applied to the readout strips. It has been demonstrated[7] that these detectors give adequate spatial resolution. Prototypes of 19.2 × 19.2 mm$^2$ sensitive area with 50 $\mu$m pitch have been tested in a high energy beam. The resolution was measured to be $\sigma$ = 8.8 $\mu$m on the p-side and 12.4 $\mu$m on the n-side. Improved resolutions are expected with this technology.

---

[6] B.S. Avset et al., IEEE Trans. on Nucl. Sci., Vol. 37, No. 3 (June 1990) 1153.

[7] L. Hubbeling et al., **Measurement of Spatial Resolution of a Double-Sided AC-Coupled Microstrip Detector,** to be published in the Proceedings of the 2nd London Conference on Position Sensitive Detectors (September 1990).

### *4.2 Vacuum Pipe*

As shown in Fig. 4. the vacuum pipe contains two thin windows, one at z ≈30 cm and one at 400 cm. A conical section with an angle of 100 mr connects the windows. The minimum aperture of the vacuum pipe will be 7.5 mrad (3 cm radius at 400 cm), so that the chambers and other detectors will have sensitive regions starting at about 10 mrad.

Construction of the vacuum chamber from aluminum or carbon fibre (or both) will limit multiple scattering of the particles and reduce interactions of particles in material near the beam. Both of these materials have been used successfully at CERN for construction of beam pipes. Recent improvements in aluminum welding used at CERN make aluminum an attractive, cost effective material for the construction of these parts where the amount of material must be minimized. Although carbon fibre is more expensive, it could provide additional immunity to secondary interactions in critical areas.

### *4.3 Magnet*

We propose to use the superconducting dipole magnet designed by Morpurgo for the NA3 experiment, and most recently used by the NA34 Helios experiment. It has a circular aperture with diameter 160 cm and a field integral $\int B \cdot dl$ = 4.6 Tesla-meter. With its magnetic length L = 2.5 m (geometrical length 3.5 m), the magnetic field is 1.84 T.

Since we do not use a septum plate in the magnet to shield the circulating beams, we need to have two beam compensation magnets, one in each arm. Our $\int B \cdot dl$ = 4.6 Tm, compared with 4.9 Tm for the UA1 magnet. Thus, the existing UA1 compensation magnets should be appropriate.

### *4.4 Pixel Detectors*

To facilitate the matching of tracks between x and y views, we intend to install pixel devices which supply space points on particle trajectories. The region between 10 and 100 mrad will be covered by a silicon pixel detector (or 45° silicon strip detector, should the pixel detector not be ready), which will be positioned just downstream of the microvertex detector on the same moveable support. The region between 100 and 400 mrad will be covered by a novel pixel drift chamber positioned just outside the first vacuum pipe window (see Fig. 4.). This chamber will also aid in tracing particle trajectories from the silicon, through the RICH counter and spectrometer. These two devices are discussed in the following sections. Monte Carlo calculations show that the resolution of the pixel detectors should be about $1 \times 1$ mm$^2$.

#### 4.4.1 Silicon Pixel Detector

The silicon pixel detector we are considering using is a prototype version of a high-rate direct readout detector which is being developed by a collaboration of U.S. industry, national laboratories and universities.[8] The design and fabrication of the first few devices is currently underway at the Hughes Aircraft Company. The overall approach is to develop a prototype readout chip separately from a p-i-n diode detector wafer. The two will be attached using the established technique of indium-bump bonding. The prototype chip contains an array of 32 x 64 pixels of size 45 $\mu$m x 150 $\mu$m and was fabricated by ORBIT in San Jose, California. The technology is 1.5 $\mu$m line width double-poly CMOS. A new version of the readout chip is scheduled to be bonded to a p-i-n diode wafer and tested during 1991.

---

[8] P.E. Karchin, **Use of Pixel Detectors in Elementary Particle Physics**; in Proceedings of Workshop on Silicon Pixel Detectors, Leuven, Belgium, 19-21 June, 1990 (in press, NIM-1991).

### 4.4.2 Pixel Drift Chambers

A front view of two cells of the pixel drift chamber (PDC) is shown in Fig 5. The sense wires of the PDC have 2 cm length and pitch 2 mm, and are approximately parallel to the outgoing tracks so that, in most cases, all ionization is collected by a single wire. The wire coordinate and its signal arrival time provide the x,y coordinates of the track. The 2-dimensional position of a track traversing the 2 cm thick gap is measured with only a left-right ambiguity.

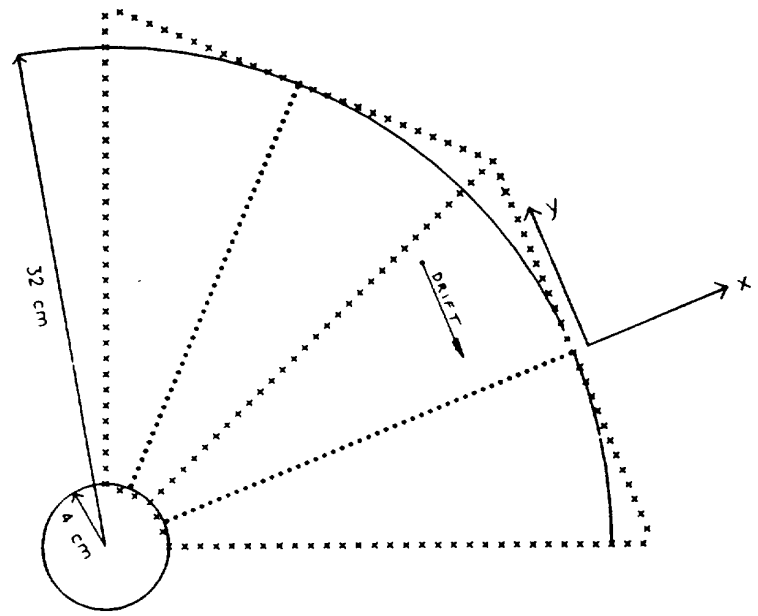


*Figure 5: Front view of one quadrant of a pixel drift chamber.*

The segmentation is determined by the requirement that diffusion not degrade the resolution beyond 1 mm. This requirement can be satisfied by a detector with an outer radius of 32 cm and a drift velocity, $v_d \approx 8$ cm/$\mu$s, if there is an 8-fold $\phi$ symmetry. The maximum drift distance is then 12.6 cm. The total number of wires in the PDC is 1120 (8 × 140).

A drift velocity value, $v_d \approx 8$ cm/$\mu$s, can be attained with a mixture of 90% methane and 10% isobutane. The diffusion coefficients are then: $\sigma_\ell = \sigma_t = 240$ $\mu$m·cm$^{-1/2}$. The pixel resolution for short drift distances is $\sigma_x = 580$ $\mu$m from the 2 mm wire pitch, and $\sigma_y = 570$ $\mu$m (assuming 6-bit TDCs). For the longest drift distances, the resolution will be somewhat degraded by diffusion effects, but not beyond the resolution goal of $1 \times 1$ mm$^2$.

### *4.5 Jet Drift Chambers*

Jet-type drift cells will be used to measure the position and direction of charged tracks. Fig. 6 shows, for example, a jet drift cell oriented so that ionization from a high-momentum 200 mrad track arrives isochronously at the 16 sense wires. Similar chambers are used by the HELIOS[9] experiment at CERN and SLD[10] experiment at SLAC. The unique requirements imposed on chambers for this proposal are the needs to minimize material near the beam pipe and to measure tracks within a few milliradians of the beam pipe.

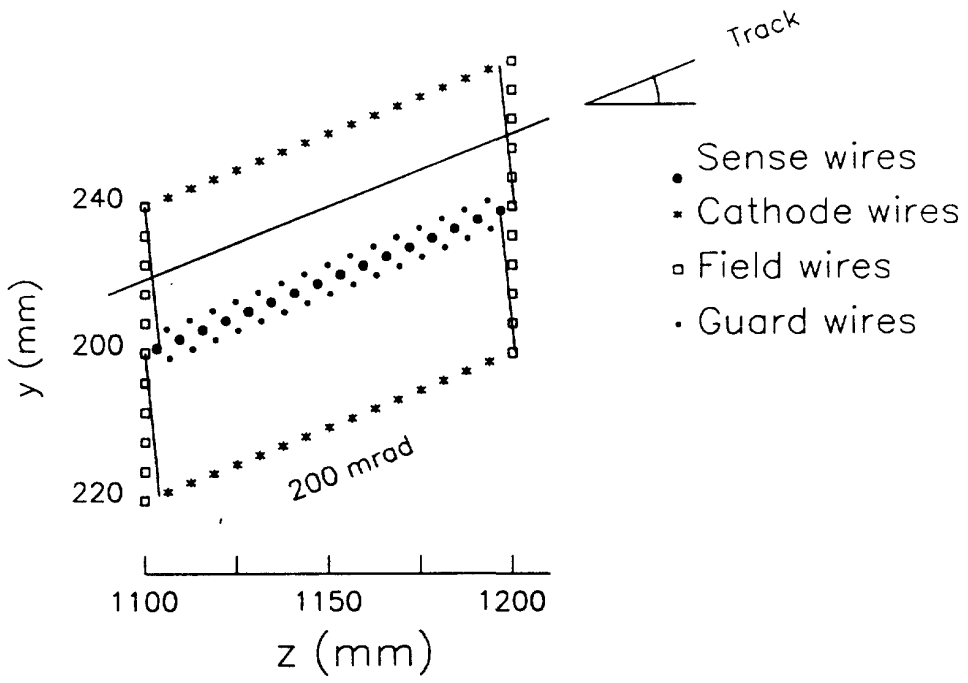


*Figure 6: A Jet drift cell in one module of Chamber 1 at θ = 200 mr.*

**Geometry of the Chambers:** Figure 4 shows the position and dimensions of the two chambers used to measure particle directions and momenta. The two chambers have similar cellular structures as summarized in Table 2. Each chamber pack is divided longitudinally into 8 modules of various cell orientations, and each module contains 16 sense wires per cell. The drift directions are x (horizontal, 0°), u (+45°), x, v(−45°), x, u, x, v.

**Cell Structure and Drift Resolution:** The drift cell geometry shown in Fig. 6 has sense wires and equipotential wires strung in planes which point to the intersection region center (x=y=z=0). Thus, the average particle direction is perpendicular to the drift direction in all cells so that charge collection

[9] D. Bettoni et al.,Nuclear Instruments and Methods A252 (1986) 272.

[10] C. Young et al., IEEE NS36 (1986).

*Table 2: Jet Drift Chamber Properties*

| | Front | Back |
|---|---|---|
| Diameter × Length ($m^2$) | 1.6 × 0.8 | 1.92 × 0.8 |
| Sense wires | 5700 | 6800 |
| Orientation (u and v are ±45°) | x, u, x, v | x, u, x, v |
| Samples per Track | 128 | 128 |
| Drift Distance (cm) | ±2 | ±2 |
| Sense Wire Staggering ($\mu$m) | 100 | 100 |
| Drift Velocity ($\mu$m/nsec) | 10 | 10 |
| Drift Field (kV/cm) | 2 | 2 |
| Gas | He/DME | He/DME |

is approximately isochronous. The wires have pitch 6.25 mm and are staggered transversely by 100 $\mu$m to help resolve the drift direction ambiguity.The maximum drift distance is 2 cm.

We intend to use a 70% Helium and 30% DME mixture because of its long radiation length (667 m) compared to that of a $CO_2$ mixture (197 m). The diffusion characteristics and drift velocity of these two mixtures are similar. The He/DME mixture results in an unsaturated drift velocity of 10$\mu$m/nsec in an electric field of 2 kV/cm with a diffusion coefficient of ~80 $\mu m \cdot cm^{-1/2}$. The corresponding maximum drift time is 2 $\mu$sec for ±2 cm cells. At atmospheric pressure this mixture will produce 21 primary electrons per cm, corresponding to 13 primary electrons per wire (with 6.25 mm pitch).

In order to estimate the expected resolution of the chambers, we note that the HELIOS chambers, using a 90% $CO_2$ and 10% ethane gas mixture, has a smaller drift velocity than will the He/DME mixture we propose to use. In order to optimize track separation and reduce space-charge, HELIOS uses field wires to limit the length of the charge segment collected by a sense wire, thus obtaining a more isochronous charge collection. Their electronics makes use of pulse clipping and shaping, and multihit TDCs. In a test beam, they found a resolution of 60 $\mu$m averaged over the 2 cm drift distance, and a 600 $\mu$m two track separation. The SLD collaboration used 92% $CO_2$ and 8% isobutane and a cell geometry which collected 16 primary electrons per sample. Their average drift distance resolution is 55 $\mu$m in ±2.5 cm cells.

Since our chambers will have substantially larger dimensions and, in the case of the first chamber, will operate in a large magnetic field, we expect a final accuracy of 100 $\mu$m averaged over the drift distance, and a two track separation of 3 mm.

**Electronics:** Low noise preamplifiers are mounted directly on the chamber frame. Two stage amplifiers with 2 nsec clipping and integration (1/t cancellation) are located in racks near the chambers. Discriminators (with thresholds set at 2 electrons on the sense wire) drive 8-bit TDCs with multihit readout. No pulse amplitude analysis is performed.

**Momentum Measurement:** The spectrometer aperture can be divided into three distinct angular regions which have different momentum measurement characteristics:

**100 to 200 mrad:** Tracks in this region traverse the entire magnet and are measured in both chamber packs. In general, the error in the measurement of a track direction, $\theta$, by a chamber pack is given by the relation

$$\sigma_\theta = [\,(\sigma_x/L)^2 \cdot (12/N) + (.01/p)^2 \cdot (L/X_0)\,]^{1/2}$$

where $\sigma_x$ is the accuracy of a single drift cell measurement and L is the distance over which the uniformly distributed N measurements are made and $X_0$ = 667 m for the He/DME mixture.

In each of the chambers of the spectrometer, we have the equivalent of 96 measurements in the bending plane (the 64 u- and v-view measurements are equivalent to 32 additional x-view measurements) over 80 cm of track length with a single hit accuracy of 100 $\mu$m. This gives:

$$\sigma_\theta = 44\ \mu\text{rad} \cdot [1 + (p_2/p)^2]^{1/2},$$

where $p_2$ = 7.9 GeV is the momentum below which the multiple scattering term dominates. The error on the spectrometer momentum measurement is given by the dipole magnet constant

$$k_2 = \sigma_p/p^2 = 4.5 \cdot 10^{-5} \cdot \cos\theta \cdot [1 + (p_2/p)^2]^{1/2}$$

for the 4.6 Tm magnet [ where we have used $\sigma_p/p^2 = \sqrt{2}\,\sigma_\theta\ /\ (0.3 \int B\cdot dl)$ ].

**10 to 100 mrad:** Tracks in this region traverse the entire length of the magnet in the vacuum pipe and are measured by the second chamber pack and the silicon, or possibly only by the second chamber pack. We find that in either case, we obtain similar resolution and show the calculation which assumes that only the vertex point is known in front of the magnet.

Assuming the small angle and thin lens approximations, the bending angle of a track with initial position, $x_0$, and final position and angle, $x_w$ and $\theta_w$, is:

$$\theta = (x_w - x_0 - z_w \cdot \theta_w)\ /\ z_m,$$

where $z_m$ is the z position of the center of the magnet, and $z_w$ is the z position of the vacuum pipe window. The momentum resolution is thus dominated by the jet chamber angular resolution or, in the case of low momenta, by the multiple scattering in the window. With a 500 $\mu$m carbon-fiber window, the resulting resolution is:

$$k_1 = \sigma_p/p^2 = 5.7 \cdot 10^{-5} \cdot [1 + (p_1/p)^2]^{1/2}$$

where $p_1$ = 16.4 GeV is the momentum below which multiple scattering dominates.

**200 to 400 mrad:** The momentum measurement of particles in this region relies on measurement of the track sagitta in front chamber pack only. The resolution in this case is given by the Gluckstern formula:

$$k_3 = \sigma_p/p^2 = (0.3 \int B\cdot dl)^{-1}\,[(720/N+5)\,\sigma^2_x/L^2 + 0.0002L/(X_0p^2)]^{1/2}$$

$$= 7.5 \cdot 10^{-4} \cdot [1 + (p_3/p)^2]^{1/2},$$

where $p_3$ = 1.46 GeV is the momentum below which multiple scattering dominates.

The results of these calculations are summarized in Fig. 7, which shows $\sigma_p/p$ vs. momentum for the three angular regions. For the trajecteries of about 90% of all tracks, the resolution of the proposed spectrometer is comparable to or better than that of the spectrometer studied in proposal P238. We therefore believe that the invariant mass resolution should be at least as good as that found in P238 ($\sigma$ = 25 MeV). Nonetheless, we are repeating the Monte Carlo calculations of P238 and will provide this information to the DRDC as soon as it is available.

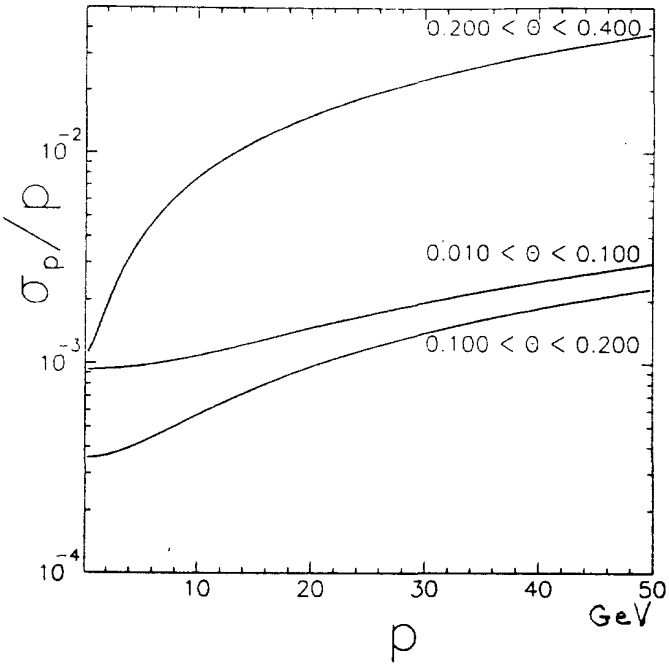


*Figure 7: Calculated $\sigma_p/p$ vx. Momentum in the Three Angular Ranges.*

## *4.6 Ring Imaging CHerenkov (RICH) Counters*

**Geometry and Photon Detector:** The RICH detectors are designed to identify most hadrons from B decays as well as leptons with momenta below about 10 GeV. The spectrometer aperture is covered by two $C_6F_{14}$ freon liquid radiators of 15 mm (front) and 25 mm (back) thickness and two $C_5F_{12}$ freon gas radiators of 500 and 750 mm path lengths, respectively. Fig. 8 shows the momentum ranges of $3\sigma$ separation for the indicated particles in the liquid and gas RICH counters. These ranges are further discussed below and shown in Table 3.

The liquid and gas radiator geometries are shown in Fig. 4 and the proposed RICH detector geometry is shown in Fig. 9. The liquid radiator is contained by a 3 mm thick fused quartz window followed by a 15 (or 25) cm Helium-filled flight path to its photon detector. This is immediately followed (back-to-back) by the gas image detector. Each detector consists of a 3 mm thick fused quartz window whose inner surface is coated with 100 $\mu$m wide metallic strips with 1 mm pitch (10% opacity) which serve to define the equipotential surface, $V_0$. Cherenkov photons impinge upon the CsI/TMAE reflective photocathode[11] which is deposited on the pad structure shown in Fig. 9. The distance between the window and the pads is 3 mm and is filled with 80% methane and 20% hexane at atmospheric pressure. Amplification is obtained on 20 $\mu$m diameter wires with 1 mm pitch placed 0.5 mm above the pad plane. The measured[12] pad efficiency for single photoelectrons exceeds 95% and the detector should be stable for gains up to $2 \cdot 10^6$.

---

[11] J. Seguinot et al., **Reflective UV Photocathodes with Gas Phase Electron Extraction: Solids, Liquids and Adsorbed Thin Films;** CERN-EP/90-88 and NIM A297(1990)133.

[12] R. Arnold et al., **Experimental Study of a Fast Photon Detector with Pad Readout,** CRN/HE90-05 (available in French at CRN, Strasbourg – English version for NIM is in preparation).

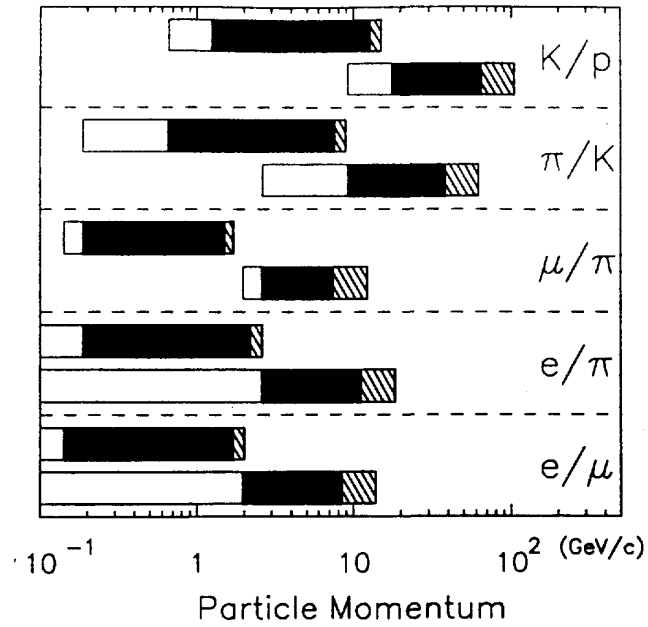


*Figure 8: Momentum Ranges of RICH Counter Identification.* For each indicated pair of particles, the upper bar is for the the liquid counters and the lower bar is for the gas counters. The open part of the bars show the momentum range between the thresholds for the lighter and heavier particles. The $3\sigma$ separation upper limits are indicated by the right end of the solid bar for front counters and right end of the hatched bar for back counters.

Secondary electron (feedback) production from the gas phase cannot occur since the TMAE partial pressure is negligible (i.e., TMAE gas flow is not necessary once the cathode has been sensitized). The primary avalanche process produces photons which irradiate the CsI/TMAE cathode and produce secondary avalanches. These pulses, however, merge with the primary avalanche because the amplifying wire is so near the cathode (i.e., 0.5 mm = 10 ns). The presence of hexane (with methane as the amplifying gas) defines the upper energy limit of the detector response (e.g., 7 eV) and provides an absorber for the $C^*$ emission lines at 7.47 and 7.95 eV (i.e., 166 and 156 nm). The $C^*$ emission line at 6.42 eV (193 nm) is then the only remaining source of feedback instability and has the same level of photon feedback as a TEA-based photoionizing gas detector. This is because the 156 and 193 nm lines are emitted with the same probability and because the quantum efficiencies of TEA and CsI/TMAE are similar at these respective wavelengths. A TEA pad detector with amplifying wires 0.5 mm from the pad plane has been successfully tested[12]. It showed enhanced stability to photon feedback and attained a gain of $2 \cdot 10^6$. It appears that the CsI/TMAE photocathode is suitable for fast operation ($\sigma_t$ = 10 ns) in the less dispersive energy range (6 to 7 eV), compatible with fused quartz windows.

The detector response parameter is $N_0 = (370\ eV^{-1}cm^{-1}) \cdot \Delta E \cdot \epsilon$, where $\Delta E$ is the energy bandwidth of the detector and $\epsilon = \int(Q \cdot T \cdot R)\ dE/\Delta E$ is the energy average of efficiencies (Q = quantum, R = reflectivity and T = transmissivity). Taking experimental values of R = T = 0.8 and an average Q = 27.5% (i.e., 12% at 6 eV and 43% at 7 eV), the detection efficiency $\epsilon$ = 0.176 and the resulting response parameter, $N_0 = 65\ cm^{-1}$.

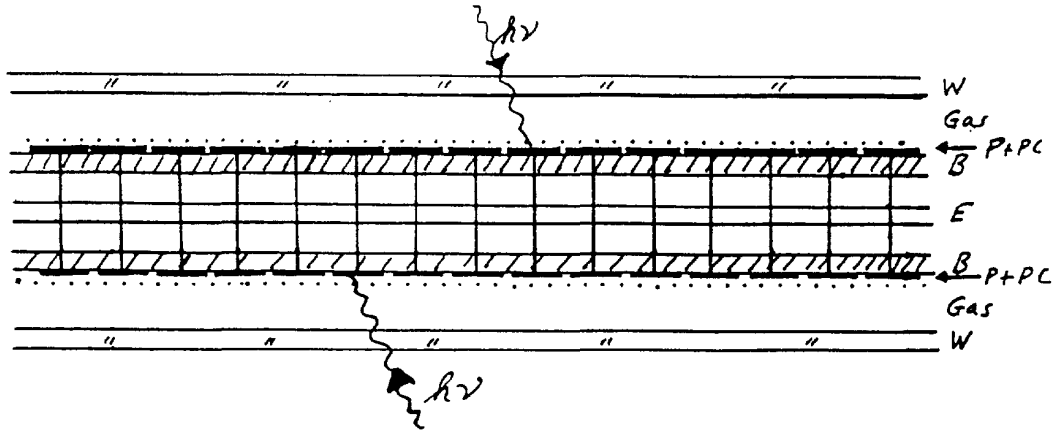


*Figure 9: Back-to-Back RICH Detector Geometry.* A schematic view is shown of the quartz windows, W, chamber body, B, readout electronics, E, and pad-photocathode structure, P + PC. A Cherenkov photon is converted by the CsI/TMAE reflective photocathode. The produced primary photoelectron is amplified on a wire and induces a signal on nearby pads. The electronics readout is common to both chambers. The gas filling is 80% Methane and 20% Hexane at atmospheric pressure.

The RICH detector surface area of both front and back counters is 1.12 $m^2$ for a total of 2.24 $m^2$. The surface area of the readout pads will be .09 $m^2$ for the front counter and .04 $m^2$ for the back counter. Thus, the total number of readout pads is $4.06 \times 10^5$. The VLSI pad readout electronics[13] comprises a fast (25 ns) bipolar analogue chain (preamplifier, discriminator, pipeline and memory), followed by a 50 MHz CMOS 2-dimensional shift register with priority encoding, zero suppression and output bus arbitration. A prototype system reads out $10^4$ pads in less than 300 ns. The first production chips have recently been tested with partial success. A second test production run with a revised layout is underway. Production of about $4 \cdot 10^4$ channels of electronics is scheduled for spring 1991 for use in a full-scale liquid RICH counter test.

**Resolution and Particle Separation Ranges:** The upper limits for particle identification in the gas are determined by the Cherenkov angular resolution $\sigma_\theta$. The relevant variables ($v_i$) are the photon emission distance along the particle trajectory in the radiator, $z_e$, the particle impact parameter relative to the mirror center of curvature, $x_e$, the photon detection point, (z,x,y), the photon energy E and the particle direction $\theta_p$ relative to the detector normal. The values and estimated errors of these parameters are summarized in table 3 for the four RICH counters. The errors combine[14] to give the total

---

[13] See Figs. 34-41 in: J. Seguinot, **Fast RICH Detectors for LHC/SSC/ELOISATRON,** Proceedings of the Symposium on Particle Identification at High Luminosity Hadron Colliders, Fermilab, Batavia, IL, 5-7 April 1989 (Ed. T.J. Gourlay and J.G. Morfin), pps. 215-253 and 671-683.

[14] T. Ypsilantis, CERN-EP/89-150;
**Particle Identification at Hadron Colliders,** Proceedings of Symposium on Particle Identification at High Luminosity Hadron Colliders, Fermilab, Batavia, IL, 5-7 April 1989 (ed. T.J. Gourlay and J.G. Morfin) pps. 133-158;
**Particle Identification at Hadron Colliders, ECFA Study Week on Instrumentation Technology,** Barcelona, Spain, 14-21 September, 1989, CERN 89-10, Vol. 2 (ed. E. Fernandez and G. Jarlskog) pps. 661-674.

Cherenkov angle errors ($\sigma_\theta$) also listed in the table.

The momentum, $p_{n\sigma}$, at which particles of mass $m_1$ and $m_2$ are discriminated at the level of $n_\sigma$ standard deviations is given by the formula:

$$p_{n\sigma}^2 = (m_2^2 - m_1^2) / (2n_\sigma k_T)$$

where

$$k_T = n \cdot \sigma_\theta / \sqrt{(N_0 L)}.$$

Values for $k_T$ which assume $N_0 = 65\ cm^{-1}$ and the $3\sigma$ momentum discrimination limits ($p_{3\sigma}$) are also included in Table 3. See also Fig. 8.

Experiments with the DELPHI barrel RICH prototype[15] have demonstrated ring images with 25 photoelectrons per liquid image (L = 1 cm), corresponding to $N_0 = 65\ cm^{-1}$ for the detector band base width $\Delta E$ = (7.1-5.6) eV. With $\sigma_\theta$ = 4.6 mrad, $N_0 = 65\ cm^{-1}$, L = 1 cm and n = 1.278, the Cherenkov constant, $k_T = 7.3 \times 10^{-4}$. Hence, particles are discriminated in this prototype at a level ($n_\sigma > 3$) up to momenta p = 1.6 GeV for $e\mu$, 2.1 GeV for $e\pi$, 1.4 GeV for $\mu\pi$, 7.1 for $\pi$K and 12.1 GeV for Kp.

[15] R.Arnold et al., NIM A270, 255 and 288 (1988).

*Table 3:* *RICH Resolution and 3σ Momentum Identification Limits*

| | LIQUID 1 | | LIQUID 2 | | GAS 1 | | GAS 2 | |
|---|---|---|---|---|---|---|---|---|
| $v_i$ | $\Delta v_i$ | $\sigma_\theta$(mr) | $\Delta v_i$ | $\sigma_\theta$(mr) | $\Delta v_i$ | $\sigma_\theta$(mr). | $\Delta v_i$ | $\sigma_\theta$(mr) |
| $z_e$ | 10 | 3.93 | 10 | 2.34 | 500 | 0.02 | 750 | 0.02 |
| $x_e$ | – | – | – | – | 1.0 | 0.00 | 1.0 | 0.00 |
| z | 0.0 | – | – | – | – | – | – | – |
| x,y | 3.0 | 1.10 | 2.0 | 0.43 | 3.0 | 1.22 | 2.0 | 0.54 |
| E (eV) | 1.0 | 2.63 | 1.0 | 2.63 | 1.0 | 0.22 | 1.0 | 0.22 |
| $\theta_p$ | 1.0 | 0.18 | 1.0 | 0.18 | 1.0 | 0.18 | 1.0 | 0.18 |

| | LIQUID 1 | LIQUID 2 | GAS 1 | GAS 2 |
|---|---|---|---|---|
| $\sigma_\theta$(total) | 4.98 | 3.58 | 1.75 | 0.80 |
| $k_r(10^{-6})$ | 656 | 471 | 25.9 | 9.68 |
| $p_{3\sigma}(e\mu)$ | 1.7 | 2.0 | 8.4 | 13.8 |
| $p_{3\sigma}(e\pi)$ | 2.2 | 2.6 | 11.2 | 18.4 |
| $p_{3\sigma}(\mu\pi)$ | 1.5 | 1.7 | 7.4 | 12.2 |
| $p_{3\sigma}(\pi K)$ | 7.5 | 8.9 | 37.9 | 62.0 |
| $p_{3\sigma}(Kp)$ | 12.7 | 15.0 | 64.0 | 104.7 |

These 3σ momentum discrimination limits are shown in Fig. 8. All angles are given in mradian, all distances in mm and all momenta in GeV. The error in the conversion point, z, is zero, because it is localized on the thin photocathode. $\sigma_\theta$(total) is the weighted sum of errors, $k_r$ is the Cherenkov constant and $p_{3\sigma}$(ab) is the 3σ discrimination momentum between particles a and b.

## *5. RESOURCES & COSTS*

The outside collaborating institutions will be responsible for the construction of all detector elements, silicon, wire chambers and RICH counters, and the trigger processor systems. We estimate these costs to be:

| | |
|---|---|
| Chambers | $1.8 \times 10^6$ SF |
| RICH System | $1.1 \times 10^6$ |
| Silicon | $0.5 \times 10^6$ |
| Processor & DAQ | $0.4 \times 10^6$ |
| Laser Alignment | $0.1 \times 10^6$ |
| Subtotal | $3.9 \times 10^6$ |
| Contingency (20%) | $0.8 \times 10^6$ |
| **TOTAL** | **$4.7 \times 10^6$ SF** |

The chamber cost estimates are based on 100 SF/wire (× 12,500 wires) plus allowances for the Pixel Drift Chambers and gas system, etc. The RICH cost estimates are based on a 250,000 pad system (50K forward RICH and 200K rear RICH) times 2 SF/pad for electronics, plus 600 KSF allowance for the mechanical structures. The silicon costs are based on a 16-plane system (64 double-sided detectors) and a cost of 5 KSF/detector. We assume that no new VLSI development will be necessary for the low-rate 1993 run. No costs are included for the pixel silicon detector since, if it is used, it would be provided by new collaborating groups.

We would like to request financial support from CERN for the following items:

(1) Displacement of the magnet, cryogenic and power supply systems and installation in LSS5.

(2) Design & Fabrication of new Roman pot mechanisms.

(3) Vacuum pipe system.

(4) Detector support structures.

(5) Implementation and use of the former UA1 beam compensation magnets.

We are in the process of determining the costs of these items in consultation with CERN staff members and will communicate these costs to the committee as soon as possible.

In addition, we would like to request that CERN provide some personnel support, in the form of per diem, for visitors from eastern European countries.

## APPENDIX A: DATA DRIVEN TRIGGER PROCESSOR SYSTEM & DATA ACQUISITION

The Level-1 trigger algorithm from Proposal P238, which consists of calculations on the silicon strip data, is divided into the following sections:

- **Line-Finding:** Lines are found in all sets of three consecutive planes of the silicon detector system, which is positioned symmetrically with respect to the interaction region center.

- **Duplicate Rejection:** If a single track is found in more than one detector triplet (this will occur whenever a particle traverses more than three detectors in a single view) the duplicate entries are removed from the list of tracks. In each such case, only the track defined by the first three planes the track traverses will be retained.

- **Vertex z Estimation:** The z position (defined to be along the beam axis) of the vertex is estimated by projecting all the found tracks to $x=y=0$. The resulting z positions are histogrammed, and the vertex is assumed to be at the peak bin.

- **Bad Track Removal:** All tracks are demanded to have an impact parameter of less than 1 mm. Most tracks which fail this cut are fake, mis-measured, or decay tracks from strange particle decay (the great majority of tracks from beauty or charm decays have much smaller impact parameters). Events with a large number of tracks failing this cut are likely to contain multiple interactions and are rejected.

- **Vertex Calculation:** A new vertex position is calculated which minimizes the sum of the squares of error-weighted impact parameters for all the remaining tracks. If the $\chi^2$ is less than some cut value, the event will be considered to contain only a single primary vertex, and will thus be rejected by the trigger.

- **Worst Track Rejection:** If the $\chi^2$ is greater than the cut value, the track with the largest contributing term is removed from the track list, and the vertex calculation step is repeated. If the $\chi^2$ test still fails after two or three tracks have been removed, the event is written out on tape or, in the LHC experiment, sent to the Level-2 Trigger Processor.

The demands made on the readout system and trigger processor by the proposed experiment are particularly severe. The lack of an effective fast trigger criterion that can be calculated in less than the time between interactions means that, for each interaction, all detector information must be read out and stored in a pipeline until the Level-1 trigger decision is taken. Moreover, in order to minimize the number of events in the pipeline, the estimated $10^4$ instructions per event needed for the Level-1 trigger algorithm must be made in the shortest possible time, say 15 $\mu$sec. An additional requirement is that the fewest number of processors should be used, in order to minimize the complexity of the channel used to distribute the data from the detectors to the processors. At the LHC, running with a luminosity of $10^{31}$, the total required computing power of the Level-1 trigger processor is given by an inelastic interaction rate of about 700 KHz times an estimated $10^4$ instructions per event, or 7000 MIPS (million instructions per second). In our proposed 1992 and 1993 runs, with relatively small luminosities, the demands are much weaker. Typical inelastic interaction rates will be about 15 KHz.

The Level-1 algorithm will be implemented using a processor with Data-Flow architecture with the processing elements imbedded in the data readout channel. The algorithm is precisely defined and amenable to implementation in hardware. Speed is of the utmost importance because it also translates directly into decreased costs for the buffer system used for the spectrometer detector information.

Five years ago, the UCLA group had a very successful experience building and using a Data-Driven processor[16] with 240 MIPS capability. This device, which was built for a Level-1 trigger for experiment UA8 at the CERN $Sp\bar{p}S$-Collider, illustrates the power of such architectures. This processor used 40 modules of two types to calculate the momentum and intercept of fast protons traversing the UA8 roman pot spectrometers. The TDC readout, calculation and final trigger decision were made in 1.4 $\mu$sec, of which only $\approx$450 nsec was used for the actual calculation.

The Data-Driven processor designed and built by the Nevis-Univ. Massachusetts group[17] for Fermilab experiment E690 is a much more powerful system and could provide our necessary online computing power. Thus, we have undertaken an R&D project to build and interface a version of their processor to our silicon system and test it during 1991. It is extremely cost-effective compared to, for example, a RISC processor farm of similar power. The processor configuration for our application is about 20% the size (in number of modules) of the configuration in use by E690 and should be relatively straight forward to build.

With time, we plan to update the technology to include optical fiber data transmission, application specific integrated circuits (ASIC's), Digital signal processors (DSP), etc. Improvements in speed, flexibility and reliability will be sought for the LHC application.

Both the readout system and the Level-1 trigger processor are pipelined. Data read from the spectrometer detectors are transferred to FIFO memories in a high speed data transport system, while the silicon vertex detector data enter the first stage of the data-driven processor described in the next section. Data entering the first stage of the processor are processed and sent on to the following processor segment. This frees the starting set of processor modules for the subsequent event. The results of the trigger calculation are used to direct the transfer of data through the transport system. Events emerging from the transport destination modules are sent to a VME-based data acquisition system for writing to Exabyte tape cartridges. At the LHC, the events will be sent to a system of RISC processors for further Level-2 processing, as well as data monitoring and recording.

**Level-1 Trigger Processor**

Briefly, the properties of a Data-Driven Processor, as exemplified by the Nevis-Univ. Mass. system are:

- **No centralized control:** There is no CPU in the system. The processor consists of a network thof function modules, in which the arrival of data at a module initiates its operation.

- **Parallel:** Several data streams are processed in parallel. In our case, track finding in the silicon detectors is done in parallel in 8 identical processors (4 quadrants × 2 views). Other parallelism can be intrinsic to a processor structure.

- **Pipelined:** Several events are in the processor simultaneously. For example, with an interaction rate of 600 KHz and an event processing time of about 15 $\mu$s, about 10 events would be in the pipeline at a time.

- **Synchronous:** All registers in the system are latched simultaneously by a 40 MHz central clock.

---

[16] J.G. Zweizig et al.(UA8 Collaboration); Nucl. Instruments & Methods A263 (1988)188.

[17] W. Sippach et al., IEEE Trans. Nucl. Sci., 27 (1980) 578;
E.P. Hartouni et al., IEEE Trans. Nucl. Sci., 36 (1989) 1480;
B.C. Knapp, Proceedings of 4th Pisa Meeting on Advanced Detectors (1989), Nucl. Instr. & Meth. (in press - 1989)

- **Expandable:** The processor may be increased to solve an arbitrarily complex problem by the addition of more modules. Since there are no resources like central memory or common I/O paths, bottlenecks do not appear. Also, because there is very little overhead, an increase in the number of processor modules yields an increase in processor speed. This will be a very valuable attribute in the future, when there will be a need to upgrade the data acquisition system to handle the higher luminosities which will be available at the new proton-proton colliders.

The processor modules are themselves quite simple. Each module takes one or two 24 bit (16 data + 8 control) input data words, performs some simple operation on them and produces an output which is passed on to the next module. All modules in the system are clocked synchronously and the input and output data words are latched into registers on each clock cycle. Care has been taken to provide access to all of the input and output registers in the system, either for reading data or inserting data. This greatly simplifies the task of debugging and diagnosing problems, since the state of the system can be determined and checked on a cycle by cycle basis.

Fig. 10 is a block diagram of the processor. There are five subroutines shown, which are isolated from each other by control buffers. By way of example, we now discuss the 3-plane line-finder in some detail. In the full LHC experiment, there will be 8 such identical processors operating in parallel (corresponding to 4 quadrants × 2 views). For the proposed $S\bar{p}pS$ runs in 1992 and 1993, the rates are such that we should be able to run with only two line finders.

**Line-Finder**

Of the subroutines listed above, the track finding step is the most complex, and provides the greatest challenge for optimal design and construction. Fig. 11 shows a diagram of this subroutine, which uses the processor modules in a configuration similar to that used by FNAL experiment E690. Depending on the required throughput, the line-finding may be performed by a single set of modules which would process each detector triplet in succession, or by many similar sets, each of which would perform the line-finding in one or a few plane triplets. With multiple independent line-finders, the effective throughput is increased by the same factor as the number of line-finders.

The following is a somewhat simplified description of the operation of the line-finding subroutine illustrated in Fig. 11. Hit strip addresses enter on the readout bus. Data from different detectors in the same quadrant appear on the same bus, and are distinguished by a 4-bit identification field (Tag). The **Buffer** modules (Labeled B in Fig. 11) select the hits from a single detector, and store them in a First-In-First-Out (FIFO) memory for eventual retransmission into the remainder of the subroutine. The hits from the first and third planes of a detector triplet are then associated into clusters by the **Associator** (A) modules and entered into lists in the **List** (L) modules. In addition, as cluster positions are entered into the lists, they are counted by the **Index Generator** (I) module. The **Index Generator** starts immediately to generate all pairs of indices of clusters in the lists. Each generated index pair causes the two **List** modules to output the cluster positions specified by those indices. The positions are then multiplied by a constant in the **Normalizer** (N) module and added together ($\oplus$ module) resulting in a prediction of a hit position in the second plane of the triplet. If there is a hit in the second plane corresponding to the value thus predicted, it is taken to indicate the existence of a track, and the hits which define the track are added to a track list. This last function is performed by a **Map** (M) module which saves the hits from the second plane in an internal bit map. It then uses the incoming hit predictions to fetch the hits in the region of the prediction. The **Table** (T) module which follows the **Map** determines whether the neighboring hits meet the track acceptance criteria by table lookup. The hits from the first and third planes associated with the accepted lines are added to the list by the **List Counter** (Lc) modules. The resulting list of hits on tracks is then entered into buffers for use by the subsequent stages of the processor.

The final translation of the algorithm described above into a hardware configuration is now being made using emulation and analysis of the processor's response to the silicon data obtained in 1990 Collider run. Preliminary design work indicates that the processor will contain about 130 modules, in addition to those in the line finders. Thus, the total is small compared to about 700 modules in the

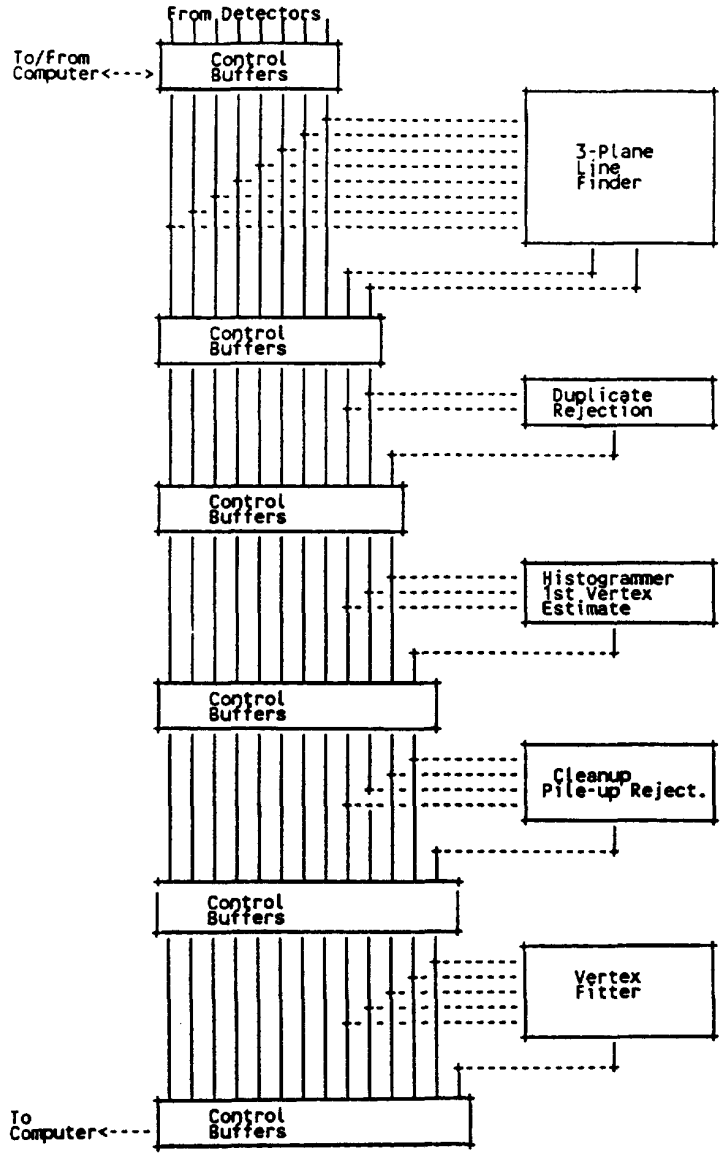


*Figure 10: Block Diagram:* Level-1 Trigger Processor with Data-Flow Architecture

E690 processor. Almost all module types already exist and are in use by the E690 Collaboration. The remaining 1-2 modules are simple extensions of the existing architecture.

**Processor Emulator**

The operation of the entire processor structure is being emulated in software. The processor emulator is a package designed to duplicate in software the action of the processor on a cycle by cycle basis. A FORTRAN subroutine is written for each type of module, of which there are about 20. One subroutine call corresponds to one clock cycle.

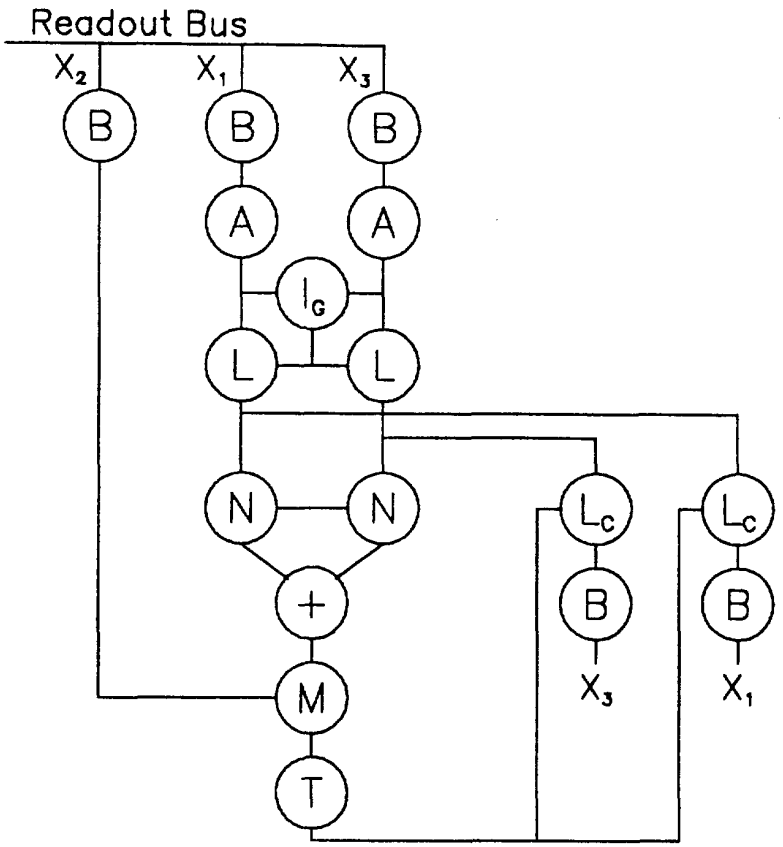


*Figure 11: Block diagram of the Data-Driven Line-Finder.*

A processor algorithm consists of a list of boards, the specification of the contents of any memory elements on those boards and the specification of how these boards are cabled together. Such a list is known as a **Configuration File.** The emulator reads this file in its initialization phase and thus determines which board subroutines are to be called. It calls these subroutines, which in turn reserve enough memory to hold any tables which must be down-loaded as well as memory locations for the input and output registers. Storage is also reserved to hold cable contents and pointers are set up to the memory locations which hold the contents of the input and output cables. After this initialization phase, the memory locations, reserved to hold on-board tables, are loaded by simulating the cycles that would be executed by the processor hardware in performing this function.

After the initialization phase, the emulator is ready to process data. Data is loaded into the locations which correspond to the input cables and the board subroutines are called as specified in the **Configuration File.** Each board subroutine checks for data on the input cables and, if present, performs its operations and modifies the memory locations which correspond to its on-board registers and output (and possibly input) cables. This procedure precisely emulates the processing performed in one clock cycle. The process is repeated for subsequent cycles until the data (and control "signals") propagate through the entire "processor" and appear in those locations which correspond to the processed data cables and the output control buffers.

Using the emulator, it is possible to precisely predict the operation of a given algorithm on any set of simulated event data. For example, the average number of clock cycles per event can be easily determined, problems of precision can be investigated and bottlenecks in the algorithm calculations can be located.

The emulator can be used not only for the design and evaluation of processor configurations, but also can serve as a powerful diagnostic tool when the same data is given to both the emulator and the hardware processor and the results of the computation compared. The operation of a single board can thus be evaluated, as can the operation of an entire subroutine.

**Level-2 Trigger Processor**

At the LHC, but not in the test runs proposed here, a second level of on-line filtering will be necessary for all events which pass Level-1. Such a Level-2 trigger will be implemented with a farm of high-speed (50 MHz or greater) RISC processors which would have access to all the data for a given event. These processors may perform the following functions:

- Perform complete track reconstruction,
- Repeat the Level-1 test with matched views, and correct weighting based on the track momenta.
- Determine the event topology.
- Aid in eliminating pileup events.

To handle the expected data rate at the LHC, we estimate that we will need a system with about 800 × 50MIPS RISC processors. Clearly, as more powerful processors become available, this number will be reduced.

## APPENDIX B: SILICON DETECTOR READOUT & INTERFACE TO DATA DRIVEN PROCESSOR

Figs. 12-13 show the block diagram of the detector readout system and the interface to the Data Driven Processor (**DDP**). The primary requirement of the readout system is to obtain the fastest possible transfer rate of event data from the silicon detectors to the data driven processor subsystem. At the same time it is necessary to retain enough flexibility to allow complete readout of all silicon channels for purposes of alignment, calibration, and analysis of the detector and SVX characteristics. Fast transfer rates are achieved by ignoring all analog data and only reading the sparsified addresses of hit strips through multiple parallel data paths. The system also has the capability of reading all channels, hit or not, including both digital and analog information at a reduced rate.

The principle features of our design are summarized below:

- **Parallel readout of all 48 detector planes.**
- **Fast (sparse) SVX readout of only the addresses of hit strips.**
- **Optional readout of both digital and analog information, either sparsified or not.**
- **Multiple readout of same event using different modes.**
- **FIFO memories to allow overlap of data transfer and SVX readout and for buffering of multiple events.**
- **Local analog to digital converters at the detectors.**
- **Non-digitized analog outputs for testing and diagnostics.**
- **Direct readout of event data, bypassing the Data Driven Processor**
- **Offline processing of pre-recorded data is possible.**

The existing silicon detector assembly, which will be used in the 1992 run, consists of 48 silicon detectors each containing 896 active strips spaced 50 microns apart. The 48 planes are organized as eight views of six parallel detectors with X and Y oriented views paired to form four quadrants. In the 1993 run and at the LHC, the same geometry but a larger number of planes will be used. The architecture of the readout system expands naturally to accommodate a larger system.

The silicon detectors are bonded to hybrids which contain seven SVX circuits each with the capacity to read out 128 channels, giving a total of 896 channels per detector. Since the detectors operate in vacuum, passive Feedthrough printed circuit boards are used to carry the signals through the vacuum bulkhead to the outside world. Each Feedthrough Board connects to four detector assemblies, an X/Y-Right and an X/Y-Left pair of planes. There are six such planes above the beam and six below the beam, for a total of 12 Feedthrough Boards.

A Read-Out-Control Module (ROCM) is plugged directly into each Feedthrough Board. All 12 ROCMs are cabled in parallel to a single Read-Out Sequencer Module (ROSM) which generates the signal sequences required to control the event detection and readout cycle. Each ROCM also has four digital data output cables containing parallel signals for each of its four planes. These cables connect to the Read-Out Link Modules (ROLM) whose primary function is to provide the interface to the processor system. A brief description of each module is given below.

**ROSM:** The Read-Out-Sequencer Module contains a 2048 by 48-bit RAM memory which is loadable from the backplane bus. The contents of the memory is a list of sequential states of each of the 48 output bits. A sequencer with a small command set steps through consecutive memory ad-

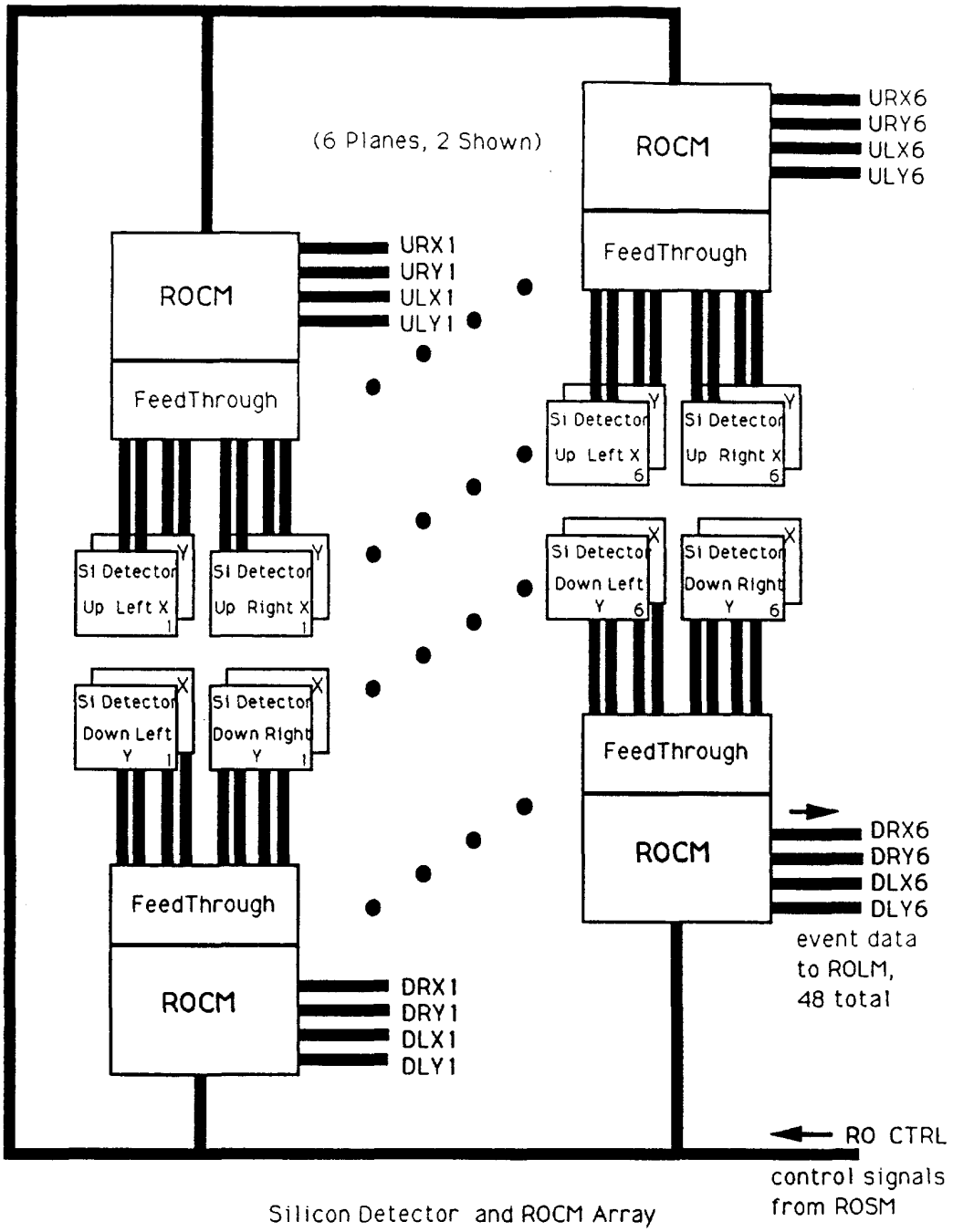


*Figure 12: Block Diagram of Detector Readout Electronics System.* 48 silicon detectors, configured as 4 quadrants, each containing an x-y pair, are readout in parallel through 12 **Readout Control Modules.** The **Readout Sequencer Module** controls event acquisition and readout via signals on the readout control cable, while event data are transferred over the 48 cables from the **ROCMs** to the **Readout Link Modules.**

dresses at a maximum clock rate of 100 nanoseconds per address. Loops are implemented using conditional and unconditional jumps and a register decrement and branch instruction. The conditional branchs are taken or not based on the state of four external inputs or four internal control register bits. The memory outputs drive the cable connected to the 12 ROCMs to provide the required signals to execute a readout cycle. The control programs and patterns are written to the ROSM memory via the VME port from the control system. ROSM operation is controlled by registers accessible via the VME bus.

**ROCM:** The Read-Out-Control Module contains the analog and digital circuitry required to detect and readout hit data from four detectors – the Right and Left X/Y pairs in a given half-plane. For each detector, there is a digital-to-analog convertor to generate charge injection to set the sparse readout hit threshold and the logic required to transmit the digital chip ID and strip address information as it is read out. The analog data is multiplexed into a single shared flash analog-to-digital converter whose output can be transmitted as part of a slow readout cycle. The analog multiplexer has additional channels to allow the charge injection DACs and the detector bias supply voltages and currents to be digitized for diagnostic purposes. The multiplexer's analog output is also available on an auxiliary connecter as an aid in diagnosing problems.

A **Priority-Out** signal indicating the end of data is available from each detector and is used as an event marker on the data output cable to the ROLM for control of the event readout cycle by the ROSM and separation of events in the ROLM.

Four different readout modes are implemented, which are the four combinations of **digital-only** or **digital and analog** with **sparse** or **full-readout.** The **digital-only full-readout** combination is available but primarily useful for diagnostics only. The fast mode reads only the SVX's digital chip ID and strip address data at the highest sustainable SVX rate. For the SVX-D version, that rate is about 200 nsec/strip. The analog output signals of the SVX are ignored. The slow readout option adds the analog information, which requires approximately 1.5 $\mu$s of settling time before digitization. An additional two clock cycles per detector are required to select and digitize each analog signal by the shared ADC.

**Full-readout** is a mode in which the analog and digital values for all channels are read out regardless of whether a hit is present or not. The SVX implements a **sparse** readout mode in which a threshold charge is injected through a capacitor directly into the integrator stage of each channel. This charge is subtracted from the integrated strip charge signal during the sampling period. If the signal is greater than the threshold, a hit is latched for that channel. Internal priority logic in the SVX suppresses the readout of channels with no hits.

**ROLM Module:** The Read-Out-Link Module provides the interface between the detector readout system and the data driven processor. It is shown implemented as a VMEbus module although other formats such as Fastbus are under consideration. The ROLM is relatively simple, providing the clocking signals, FIFO buffers, and logic to read from the ROCMs and write to the processor input buffers. The ROLM inputs are the output cables from the ROCMs. There is one input and a receiving FIFO for each of the 48 detectors allowing a fully parallel readout cycle. The outputs of the ROLMs are designed to be connected together in a daisy chain fashion with a simple grant passing mechanism to allow the FIFOs in a ROLM chain to be read out sequentially. The output is sent to the input of the Data Driven Processor line finder. The ROLM outputs may be connected in a number of configurations to match the number of line finders which are present in the DDP.

The input and output ports of the FIFO buffers are asynchronous and independent, so that one event can be read from the FIFO while another one is being written to it. An event separator bit is used to mark the end of each event in the FIFOs to maintain synchronization. The block diagram shows a six-port ROLM with fiber optics cabling to the ROCMs.

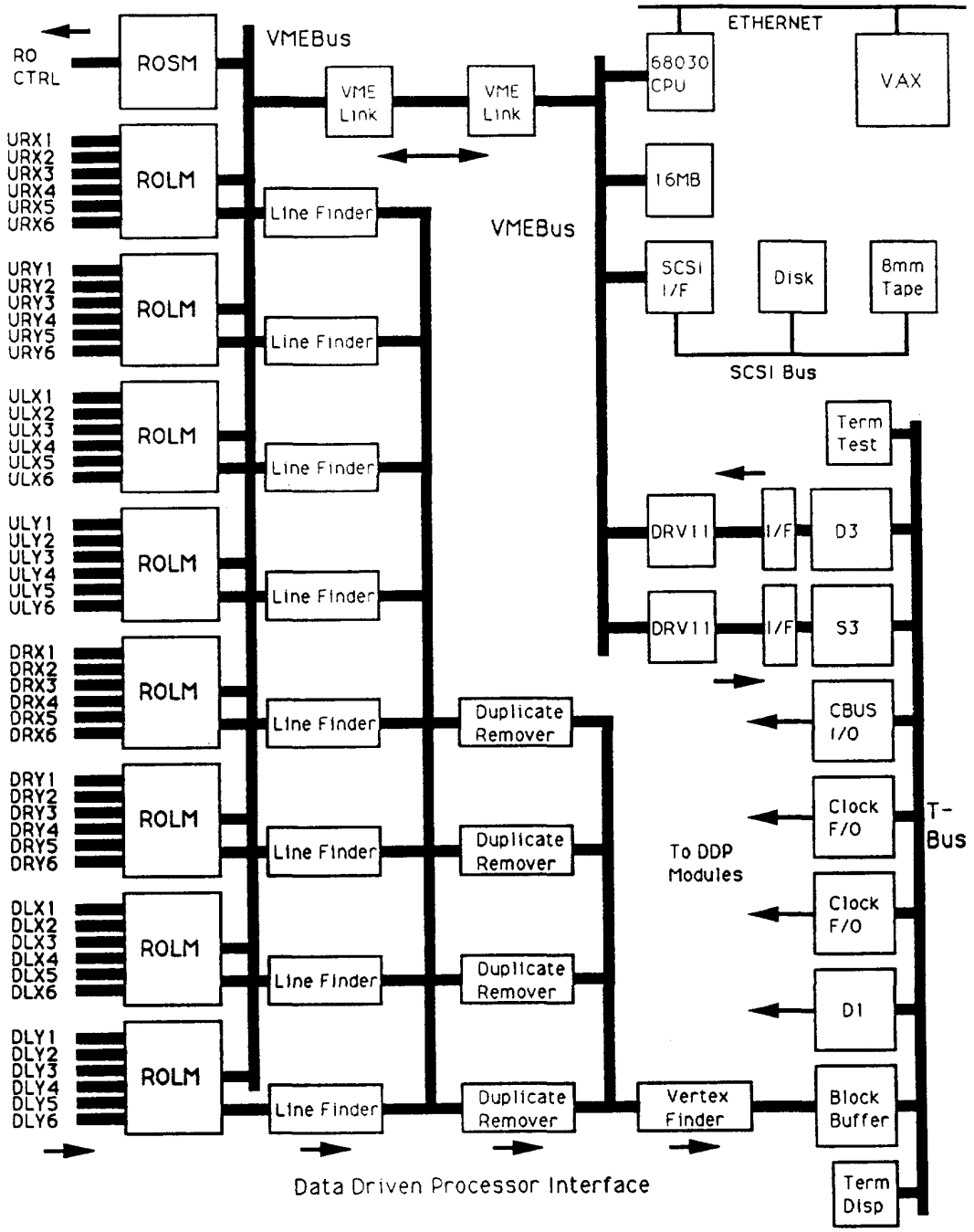


*Figure 13: Block Diagram of Detector Readout Electronics System.* Event data are received in parallel by the **ROLMs** over 48 cables from the **ROCMs**. The output of the **ROLMs** feeds the Data Driven Processor (DDP). Processed events from the DDP are transferred through the T-Bus to the VME control system and recorded on 8 mm tape. The **ROLM** VME port is bi-directional and allows event data to be read directly from the detectors, bypassing the DDP, or offline event data to be written to the DDP, bypassing the detectors.

The **Priority-Out** signals from the SVXs are brought to front panel connectors where they can be combined (ANDed) to form an End-Event signal for use by the ROSM to terminate the completed readout cycle.

The VME port of the ROLM is a read/write path and can be used to write test or offline event data to the ROLM FIFO for transfer to the DDP or to read event data from the FIFO, effectively bypassing the DDP altogether.

**Control System:** A VME subsystem comprised of a 68030 processor, 16 MByte of memory and SCSI tape and disk drives is used as the overall Event Readout System Controller. DDP control and diagnostic signals are sent from this system via DRV11 modules to the T-Bus crate, from which they are connected to the DDP. Processed DDP event data is transferred in the reverse direction for recording on tape or disk.

APPENDIX C

EUROPEAN ORGANIZATION FOR NUCLEAR RESEARCH

**DRAFT**
22 January 1991

# Development and Test of a Large Silicon Strip System for a Hadron Collider Beauty Trigger

J. Ellett, S. Erhan, P. Kreuzer[1], D. Lynn, M. Medinnis, P. Schlein, J. Zweizig
University of California*), Los Angeles, U.S.A.

A. Czermak[2], G. Engelmann, O. Klingsheim[3], K. Ley, A. Rudge, H. Wahl, P. Weilhammer
CERN, Geneva, Switzerland

G. Borreani
University of Ferrara and INFN, Italy

W. Hofmann, B. Wilkens
Max Planck Institut fur Kernphysik, Heidelberg, F.R.G.

M. Calvetti, M. Punturo
University of Perugia and INFN, Italy

Y. Guz, Y. Ivanuschenkov
IHEP-Serpukhov, Protvino, U.S.S.R.

C. Biino, S. Palestini, L. Pesando
University of Torino and INFN, Italy

R. Harr, P. Karchin
Yale University**), New Haven, Connecticut, U.S.A.

## Abstract

Large aperture forward spectrometers with planar geometry perpendicular to the beam line are the natural detectors to accomodate the expected forward peaking of heavy flavor production at high energy hadron colliders. Such systems, together with silicon strip detectors for triggering, which are configured perpendicular to and close to the beam inside the vacuum pipe at the center of the interaction region should make possible the exploitation of hadron colliders as Beauty Factories. We have designed, built and tested such a silicon system at the CERN Sp$\bar{p}$S-Collider. Running 1.5 mm from the Sp$\bar{p}$S beams, clean background-free events are seen.

To be submitted to Nuclear Instruments and Methods

---

*) Supported by U.S. National Science Foundation, Grants PHY90-08221 and PHY85-09175.
**) Supported by the U.S. Department of Energy
1) Ecole Polytechnique, Lausanne, Switzerland
2) Visitor from Institute of Nuclear Physics, Krakow, Poland.
3) Present Address: Stavanger Tekniske Fagskole, Stavanger, Norway.

# Contents



# 1 Introduction

The exploitation of hadron colliders as beauty factories would be impossible without a high resolution vertex detector and an efficient and highly selective beauty trigger. A scheme for realizing such a detector and trigger was explored and extensively modeled in the context of a proposal to the CERN SPS committee[1]. Although this proposal was for an experiment at the Sp$\bar{p}$S-collider, it was recognized that the apparatus built for the Sp$\bar{p}$S collider experiment could serve as a basis for the more elaborate apparatus needed to cope with the higher energies of the next generation of hadron colliders. Indeed, the long range goal of the collaboration is an experiment with sufficient sensitivity to measure CP violation parameters in the decay of B mesons. The attainment of this goal awaits the high luminosites and high cross-sections of the next generation of hadron colliders.

We report here on the design and construction of a test version of the proposed detector and present a preliminary analysis of the results obtained with it during the Fall 1990 Sp$\bar{p}$S-collider run. The purposes of this test were to assess the feasibility of operating a silicon detector at a few millimeters from the beam axis, and to gather data for the off-line testing of trigger algorithms based on silicon hit information, which would select events containing beauty production.

Fig. 1(a) shows a side view of the detector used for this test. Part (b) of this figure shows a perspective drawing. The detectors are organized into 6 planes perpendicular to the beam axis. Each plane has 8 silicon detectors: 4 with vertical (x-view) and 4 with horizontal (y-view) strips.

The "fixed-target" type geometry was adopted to accomodate the anticipated sharp peaking of B production in the beam directions[1]. The forward peaking of reconstructable B mesons is even sharper since the decay products of B mesons produced near Feynman-x = 0 tend to have low momentum and therefore become easily lost in pattern recognition. The detector was therefore optimized for particles traveling in the forward and backward directions, at angles less than about 600 milliradians.

In order to minimize extrapolation distance to the primary vertex, the detector was positioned at the center of the interaction region and the gap between upper and lower halves was reduced to the minimum distance consistent with clean running conditions. The detector is

mounted in a device (called a Roman Pot) which allows retraction of the detector to a safe distance during beam manipulations and setups.

The detector assembly and associated systems are discussed in Sections 1 through 5. A discussion of the performance of the detector during the collider test run and a preliminary analysis of the data taken during that run is presented in Section 6.

# 2 The Detector

## 2.1 Overview

A photograph of a detector with its associated readout hybrid is shown in Fig. 2. The assembly pictured here was appropriate for readout of the horizontal coordinate. The silicon detector is on the left in this view. The seven chips next to the detector are SVX pre-amplifier/readout chips. A Kapton readout cable is shown plugged into connectors near the right-hand edge of the hybrid.

The detectors were supported by aluminum brackets glued to the back of the alumina hybrids. Fig. 3 shows a side view of two detector planes. Each detector is shown attached to its hybrid and heat sink. The distance between adjacent x- and y-view detectors was 2 mm and the distance between the center lines of adjacent planes was 3.8 cm.

As shown in Fig. 4, the aluminum support brackets were afixed to a water-cooled mounting plate which was in turn attached to a vacuum bulkhead. As shown in Fig.s 3 and 4, a thin corrugated window separated the detector volume from the main SPS vacuum. Since the window was required to be thin, the detector volume was also evacuated.

## 2.2 Silicon Detectors

The silicon strip detectors were fabricated by the Central Institute for Industrial Research (S.I.) in Oslo and are functionally similar to those used by the DELPHI experiment[2]. They have an active area of $44.8 \times 44.8\,\mathrm{mm}^2$ and thickness $280\,\mu\mathrm{m}$. Each detector has a total of 1793 diodes with a pitch of $25\mu\mathrm{m}$, only half of which (every second one) is read out. The charge deposited on diodes between read out strips capacitively induces signal on neighboring strips, thus enhancing charge sharing and improving spatial resolution. Metal strips, which are bonded to preamplifier inputs, run the length of the diodes and couple capacitively to the underlying p-strips via a 200 nm thick oxide layer. Each p-strip is connected to a common bias bus through individual $\sim 6\,\mathrm{M}\Omega$ polysilicon bias resistors. We find more than a 99% yield of good strips and leakage currents in the range of 50 pA/strip to 1 nA/strip.

## 2.3 SVX Chips

A detailed discussion of the properties of the Lawrence Berkeley designed SVX-D chip can be found elsewhere[3]. We present only a functional description relevant to the design of the support electronics.

The SVX-D is a CMOS chip which contains 128 charge-sensitive preamplifiers with an overall gain of about 15 mv/fc as well as circuitry for multiplexing and optionally "sparsifying" pulse-height information (i.e. reading out only those strips whose charge is above a set threshold).

In addition to the 128 preamplifier inputs, the SVX has the following input/output lines:

- A set of eight bi-directional data lines which is used to read addresses of hit strips, to set and reset various switches in the pre-amplifiers, and to write a chip number during initialization.
- Three control signals which determine the function of the data lines.
- A calibration line by which charge is injected to set a threshold for sparse readout.
- Input and output priority signals which allow daisy-chaining of an arbitrary number of SVX chips.

- A gated analog line which, during readout, outputs a voltage proportional to the charge on the strip currently being read out. The analog line is only active when the chip currently has priority.

The SVX requires two sources of power, an analog power of six volts which is supplied to the bottom of the chip as well as a bonding pad, and a digital power of between five and six volts which is supplied to a bonding pad.

For each strip read out, the SVX first outputs the chip number (which is written to the chip during initialization) followed by the strip number onto the eight data lines while simultaneously outputting the analog pulse height onto a common bus.

## 2.4 Hybrid Design

Each silicon detector (896 strips) requires seven SVX chips, which were mounted on ceramic alumina hybrid circuit boards. There were two different but similar hybrid designs for the x- and y-view detectors. The two designs were needed since connections could only be made near the outer vertical edges due to space limitations.

Both hybrid types contain five main layers silk-screened onto the alumina substrate. The lowest two layers have horizontal and vertical gold traces intended to bring the control, data, calibration, and analog signals to and from the SVX chips. An SVX analog power plane, an SVX digital power plane, and then a ground plane are layered above. Dielectric material electrically isolates the various layers. Surface mount capacitors provide filtering for the SVX power. The SVX chips are glued with conducting epoxy onto an exposed section of the analog power plane. Connections to the input/output pads of the SVX chips and the gold traces on the hybrid are made via an ultrasonic wire bonding process using one mil diameter aluminum wire. Two sixteen-pin surface mount connectors manufactured by DuPont (Microflex) were mounted on each hybrid.

## 2.5 Detector Mount

The individual silicon detectors were glued to hybrids along one edge, with a two millimeter overlap. The hybrids were then glued to aluminum brackets, which also served as heat sinks, using silver-impregnated epoxy for good heat conduction. The gluing was done under microscope and on a vacuum jig with a precision of ten microns perpendicular to the strips and one hundred microns parellel to the strips. The detectors were positioned for gluing with reference to alignment holes on the heat sink and to the heat sink surface which abuts the mounting plates. Each assembled detector was attached to its mounting plate with a single screw. The x-view detectors were held in position with alignment pins.

The two water-cooled mounting plates (for top and bottom hodoscopes) each consisted of two 2 cm thick plates glued together. Before gluing, a channel for cooling water was machined into the inner surface of one of the disks and matching slots were machined into both disks for the passage of readout cables. Fig. 5 shows a photograph of a partially assembled hodoscope. Five of the six planes had been mounted at the time the photograph was taken. The x- and y-view detectors for each quadrant were mounted with diode strips facing each other across a 2 mm gap. The cable slots for the sixth (as yet unmounted) plane are visible on the right-hand side of this photograph.

Each mounting plate was attached to vacuum bulkheads by means of four precisely-machined aluminum bars. The vacuum bulkheads were made from 3 cm thick aluminum plates, which bolted onto the Roman Pot assembly (described below). Signals to and from the SVX chips traversed from vacuum to atmosperhic pressure on printed-circuit boards ("feed-through boards") which were glued with Araldite into the bulkheads. The bulkheads also contained ports for vacuum pumps and cooling water. Fig. 6 shows the same five-plane assembly pictured in Fig. 5 after it had been joined to the vacuum bulkhead. The bulkhead is at the bottom of the figure. The vacuum-side portions of the printed-circuit boards can be seen traversing the bulkhead and a cooling-water tube is visible in the forground.

## 2.6 Assembly and Testing

Upon receipt from the manufacturer, the silicon detector wafers were subjected to a thorough visual inspection at a microscope station with the intention of catching physical defects such as shorts between strips, breaks in the bias and guard rings or diffusion strips, and poorly cut wafer edges.

After visual inspection, electrical measurements were made of the coupling capacitance and the interstrip capacitance and resistance. Additionally, the leakage currents of the guard ring and bias strip were monitored for a period of 40 to 50 hours. Typically, bias strip currents were in the range $0.1 - 1.0\,\mu$amps while the guard ring currents would increase over a period of about one day from an initial value of about $1 - 10\,\mu$amps to $20 - 100\,\mu$amps and then stabilize. Approximately 10% of the detectors were rejected either for physical or electrical defects.

The SVX chips were tested at Lawrence Berkeley Lab using a procedure developed for the CDF $\mu$vertex detector. Our batch had the unusually low yield of 13% good chips. Using the test results, an attempt was made to match as closely as possible the nominal analog output voltage for each set of seven SVX chips on a given detector. No additional tests were performed on the SVX chips before mounting on the hybrid assembly.

The alumina hybrids were designed by our group and manufactured at CERN. After manufacture, they were visually inspected for obvious defects, then passive components (resistors, capacitors and connectors) were mounted. The hybrids were tested for continuity between bonding pads and connectors and for shorts between adjacent lines. The SVX chips were then glued in place and wire-bonded to the hybrids.

At this point, the hybrid assembly was tested. The test setup was similar to the experimental readout system which is discussed in Sec. 5. It consisted of a MicroVax controlling a CAMAC crate which contained a sequencer module (SRS)[4] to generate the SVX clocking signals, and a readout module (SDA)[4] to read and store the analog and digital address information from the SVX's. A test board provided the electrical interface to the detector assembly and contained a variable charge injection circuit as well as oscilloscope test points. The following checks were made:

- analog output voltage responds to charge injection onto the calibration line;
- priority propagates through the SVX chain;
- average analog outputs of most channels are correct;
- noise levels of most channels are small;
- correlated shifts of baselines (common-mode) on all channels of a chip not too large;
- no (or few) skipped, out of sequence, or multiple occurrences of digital addresses.

Problems detected by the testing were repaired, sometimes with the use of a probe station for tracking down less obvious malfunctions. Not all problems were considered serious enough to warrant the risk of creating a worse condition by attempting repairs. An example would be a channel which was always skipped during readout.

After gluing the hybrids to the heat sinks and the detectors to the hybrids, the 896 readout strips were bonded to the inputs of the SVX preamplifiers using a semi-automatic bonding machine. This process took approximately two to three hours per detector. The detector pictured in Fig. 2 does not have an attached aluminum heat sink (it was a test assembly) but otherwise shows a detector at this stage of assembly.

The above tests were then repeated with the detector attached and biased. As a final test each detector was scanned with a tightly focused, pulsed LED light source to verify that all (or most) channels responded and to get a rough measure of the relative analog gain differences between the SVX's. The detectors were then assembled onto the mounting plates as shown in Fig. 5.

# 3 Installation and Roman Pots

## 3.1 Roman Pots

The silicon detector must be isolated from the Spp̄S machine vacuum for two reasons:

1. The pressure in the vacuum system around experimental areas of the Spp̄S must be in the low $10^{-10}$ mbar range. However, the gas load ($\sim 10^{-3}$ mbar $* \ell/s$) of the complete silicon detector assembly precludes pumping to this pressure range.

2. The detector must be electromagnetically shielded from the beam bunches which set up strong image currents in the vacuum chamber walls which could cause very serious noise pickup in the detectors.

Thus, a metallic, vacuum-tight separation with low outgassing rate was needed. The separator was also required to present a minimum thickness to particles traversing the detector's active volume in order to minimize multiple scattering, particularly of small angle tracks. We therefore developed a special aluminium vacuum vessel which had a very thin ($200\mu$ m) corrugated Al-foil in the sensitive volumes of the detectors as shown in Fig. 3. Since such a thin Al-foil could not withstand the pressure difference of one atmosphere, the silicon detector assembly was designed such that it could be pumped down to about $10^{-4}$ mbar and therefore exclude all forces on the Al-foil.

For reasons of expediency, the whole arrangement, pot and silicon detector, had to be designed such that it could be fitted into the existing Roman Pot driving mechanism which is described below.

Fig. 7 shows the aluminum vacuum vessel with its two corrugated side walls. This piece was machined from a single piece of aluminum using a numerical-controlled milling machine. The free space between the two side walls, which housed the silicon detector planes, was later covered with the 200 $\mu$m thin Al-foil.

The corrugated shape of the Al-foil was produced using special tools as shown in Fig. 8 and afterwards annealed in order to stabilize the corrugated shape. It was then glued to the side walls of the pot with a special silver charged Araldite to ensure good electrical contact between the Al-foil and pot, and thus maintain adequate electromagnetic shielding. Fig. 9 shows a close-up of the corrugated region of the pot, after installation of the Al-foil.

Since the total surface of glue ($\sim 50\,\mu$m thick line over the length of the corrugated shape) exposed to the Ultra High Vacuum (UHV) system of the SPS is less than 1% of the surface of the complete pot, its contribution to the total outgassing rate is negligible. Fig. 10 shows a detail of the connection of the Al-foil to the pot.

## 3.2 Positioning Mechanism

Given the short time allowed for construction of equipment for this test, it was not possible to design and build an optimized positioning mechanism. We therefore used, with minimal compromise, an existing Roman Pot mechanism which had previously been used for diffractive measurements by two experiments at the Spp̄S-collider. A photograph of the mechanism is shown in Fig. 11.

The mechanism allows detectors, mounted inside pots above and below the beam, to be displaced along the vertical axis. The pot flanges are connected to the vacuum chamber of the machine by bellows. During beam manipulations, the inner edge of the vacuum shield was retracted to a distance of about 5 cm from the nominal beam position. During data-taking runs, the two pots were brought close to the beam axis as shown in Fig. 4. The pot position was adjusted and monitored using a linear position transducer with an accuracy better than 50 $\mu$m.

## 3.3 Pumping system

Fig. 12 shows the schematic layout of the special pumping system installed for this test. The line between the SPS sector valves VVS1 and VVS2 represents the SPS vacuum system with

the pot assembly in the center. VPRS1 to VPRS3 are turbomolecular pumps backed by rotary vane pumps. VG1, VG2 and VG-SPS are vacuum gauges and V1 to V4 are roughing valves. On each side of the pot, a combination of a 400 $\ell$/s sputter-ion with a 1000 $\ell$/s sublimation pump (VPS) was installed for UHV production.

The initial pump down from atmospheric pressure of the SPS vacuum system and of the pots down to about $10^{-1}$ mbar is made with VPRS1 via the valve V1 and V2. Below a pressure of $10^{-1}$ mbar, measured on VG2 and VG-SPS, valve V2 closes automatically and VPRS1 is pumping via V1 only the pots. At the same time V3 and V4 are opened to pump the SPS vacuum system with the help of VPRS2 and VPRS3. After a bakeout at 150 $^0$C of the SPS vacuum system, UHV production with the VPS's was started.

In case of a sudden pressure rise higher than $10^{-1}$ mbar in the SPS vacuum system or in the pots, VVS1 and VVS2 as well as the roughing valve V1 close and the separation valve V2 open in order to equalize the pressures in both vacuum systems and therefore avoid damage to the detector or thin Al-foil of the pot.

After a short power cut the pumping system restarts automatically. If there is however a slow pressure rise above $10^{-1}$ mbar due to an extended power failure of a few hours, the complete pumping system will be blocked and can, for safety reasons, only be manually restarted.

The best pressure obtained in the SPS vacuum system after a few weeks of pumping was about $5 \times 10^{-10}$ mbar with a residual gas composition mainly composed of hydrogen and water vapor. The pressure in the pots was maintained at about $5 \times 10^{-4}$ mbar.

# 4 Silicon Power System

The power system supplies the DC voltages to run the detectors, with the requirements that these voltages have low noise ($<$ 1 mV at the detector) and that every bias current is monitored. The system consists of a switch panel in the counting room for individual control of each of the 48 detectors; the supplies, mounted in a rack next to the detector; and a monitoring system composed of a CAMAC multiplexer and ADC module, read out by a Caviar unit in the counting room. The use of opto-couplers to switch individual detectors assures total electrical isolation of the control circuitry thus minimizing noise pick-up.

The SVX analog and digital voltages as well as voltages to power the PID boards (described below) were generated by commercial supplies (Ultronix).

Ninety volt batteries (Eveready No. 490) were used to bias the detector back planes, since suitably decoupled batteries provide ripple-free voltage, and make individual detector current monitoring relatively simple. Four batteries were mounted in a double-width NIM module. The output voltage for each channel could be independently adjusted in the range 0 to 90 V and was determined by a combination of an external reference voltage, common to all supplies and potentiometers for each channel as shown in Fig. 13. Two Darlington connected transistors provide a low output impedance, and independence from battery voltage changes. With typical bias voltages of 50 V and currents of 1 to 100 $\mu$A (due mainly to guard ring leakage), battery life is greater than 6 months.

The voltages and currents of all supplies were continuously monitored by a CAMAC analog scanner and DVM (Lecroy LG5310), and displayed in the counting room in bar graph form. The SVX analog and digital voltages and the detector bias voltage are interlocked to insure that they could be turned on only in the correct order.

# 5 Triggering and Readout System

The control signals necessary for operation of the SVX chips were generated by the Lawrence Berkeley designed SRS (SVX Readout Sequencer)[4] CAMAC module. This module contains an AMD2910 sequencer and 12 kbytes of program memory which may be downloaded from the host computer. Approximately 6 kbytes of the memory are used to store bit patterns which are sent to front panel outputs to drive the SVX's. The AMD2910 addresses successive locations of the internal memory to access these bit patterns, but may jump to any specified address depending

on the state of front panel input signals (e.g. scintillator trigger signal). This permits access to the different sets of bit patterns required either by the sampling sequence or by the SVX readout sequence.

The SRS control signals were converted to differential levels and sent over a 50 m flat twisted pair cable to the interaction region, where a repeater board converted them to single ended TTL levels. The control signals then traveled another two meters over two flat cables to twelve Plug-In-Driver (PID) printed circuit boards of the top and bottom half detectors. This signal path is indicated in Fig. 14 for the upper detector hodoscope. As shown in this figure, there is one PID board for each detector plane. The PID boards plug into feed-through boards which together with short Kapton cables, relay signals to and from the hybrids, through the vacuum bulkhead . Two analog output daisy-chains from each PID board are routed to the control room on shielded twisted-pair cable.

The purpose of the PID was to:

- fan out control and data signals to the hybrids;
- daisy chain the readout of the x- and y-view hybrids from each quadrant to produce two daisy-chains of 1792 channels per PID board (for a total of 24 daisy-chains);
- convert the single-ended SVX analog output signals to differential levels which are sent to the counting room via approximately 50 m of shielded twisted pair cables;
- mulitplex the digital data signals (strip number and chip number) from the SVX chips onto a bus common to all PID boards. Signals from any daisy-chain could be selected from the counting room for diagnostic purposes. (This bus is not shown in Fig. 14.)

The detector readout was triggered by a coincidence of scintillation counters, which detected particles produced at polar angles between 0.027 and 0.11 rad. The trigger was sensitive to approximately 45% of the total cross section and introduced minimal bias.

Synchronization with the beam crossing was accomplished by means of a signal from a directional coupler which sensed the beam passage. When live, the SRS generated a double-correlated sample and hold sequence for every beam bunch crossing (3.8 $\mu$sec). Upon receipt of a scintillator trigger, the SRS initiated and controlled the SVX readout.

We did not utilize the sparsification feature of the SVX since, in the short time available to us, we were not able to adequately evaluate its performance. We were particulary concerned that charge fluctuations at the inputs to the preamplifiers on time scales comparable to the readout cycle would result in common baseline shifts which would render the sparsification useless. Rather, we chose the CERN-designed SIROCCO II[5] (SIlicon ReadOut Camac COntroller) module for analog to digital conversion. This module features optional hit sparsification as well as common mode and pedestal subtraction. It contains a 10-bit flash ADC, and internal memory to store pedestals and pedestal subtracted pulse heights for up to 2048 channels. Twenty four of these modules were used (one for each daisy chain).

Readout to the host computer (MicroVAX II) was implemented using standard CAMAC and ROMULUS/REMUS modules. Silicon hit data together with pulse-height, pulse arrival time and scaler information from the scintillators were written to 8 mm tape cassettes using Exabyte tape drives.

Data was collected with full detector readout as well as under SIROCCO II sparsification. Approximately 1.4 million events were written in the full readout mode. The data acquisition rate was limited to approximately 3 Hz by the tape writing speed. The full event size was 172 kbytes.

For readout sparsification, the threshold was set at three times the average r.m.s. noise found in the two daisy-chained detectors for each SIROCCO II . Only channels passing the threshold were read out and written to tape. In order to monitor pedestal stability and common mode noise, 21 additional "monitor" channels (2% of the total), were always read out. Thresholds for hot channels were set such that those channels were never read out. The event size was typically 9 kbytes, and the acquisition rate was approximately equal to 35 Hz. About 5 million events have so far been collected in this mode.

# 6 System Performance & Data Analysis

The silicon Microvertex detector was tested under high luminosity (typically $2 \times 10^{30} cm^{-2} s^{-1}$) collider operating conditions during the Fall 1990 run. The most important result obtained from run is that it is possible to cleanly and routinely run a silicon detector at a distance of 1.5 mm[1] (approximately 15 beam widthes) from the beam.

In more detail:

1. We saw no increase in scintillator counting rates as the pot window was brought from 5 cm to 1.5 mm, indicating that the beam scrapers which were positioned at 6 beam widthes were still effectively shadowing the detector assembly. We found however, that when positioning the window to a distance of 1.2 mm from the beam, we experienced an increase in scintillator counting rates of about a factor of two, which can be accounted for if aproximately one halo track per bunch crossing interacts in the aluminum shield. Thus, we chose to run regularly at the 1.5 mm distance.

2. We saw no evidence for run-to-run variations in the average vertical position of the beams and were thus able to set the detectors to the same position at the start of every Sp$\bar{p}$S fill. Preliminary analysis of reconstructed verticies shows that over the course of a run, the Sp$\bar{p}$S beams were steady to better than 100 $\mu$m.

3. Forty seven of the 48 detectors functioned properly when installed into the Roman Pots and subjected to vacuum. The back-plane of the one failed detector developed a short to ground. Two SVX chips (256 channels) of another detector failed during the run due to a power glitch. Of the remaining 46 detectors, 386 ( 1% of remaining channels) were unusable due to high noise levels caused mainly by defects in the silicon (e.g. holes in the $SiO_2$ layer resulting in shorts between a diode and its readout strip). Therefore, a total of 96.4% of the 43008-strip system was found to work.

4. Electronic effects, such as pedestal shifts, due to RF pickup of the passing beams was not seen.

5. Total detector leakage current decreased when the detector was put into vacuum and remained low during the course of the run. Typical total leakage currents varied between 1 and 20 $\mu$amps while in vacuum. This compares to values in the range of 100 to 200 $\mu$amps as measured on the test bench in air.

6. Strip noise showed no noticable increase during the course of the run, thus no significant radiation damage was observed. This is further illustrated by Fig. 15(a) which shows the rms noise levels in units of ADC channels of a typical detector as a function of channel number. The data for this plot were taken near the end of the collider run. Since the beam passes nearest to strip 896, the radiation dose from interactions increases with increasing strip number. The fact that the rms noise shows no corresponding increase indicates that no significant interaction-induced radiation damage had occurred.

7. Based on an event scan, the number of tracks coming from a sources outside the p$\bar{p}$ interaction region (e.g. "beam halo") was neglible.

8. The detectors and associated readout electronics displayed excellent signal to noise characteristics. The average cluster[2] pulse height distribution for a typical detector is plotted in Fig. 15(b) for all clusters with width less than four strips and (cross-hatched) all clusters with width equal two. The average of the uncut distribution is 94.5 ADC counts while the average of the cluster width equal two distribution is 74.9 ADC counts. Dividing

[1] The inner edge of the aluminum window was positioned at 1.5 mm. The edge of the sensitive region of the silicon was 3.0 mm from the beam.

[2] A cluster is defined as a contiguous series of strips each with a pulse height more than 4 times the rms noise and with total cluster pulse height more than 5 times the rms of all strips in the cluster

this last value by the average rms noise shown in Fig. 15(a) of about 2.2 ADC counts gives an average signal to single channel noise of 34.0. (When no cut is made on cluster width, the average signal to single channel noise is 43.4 but there is evidence for significant contribution from hits originating from two nearby tracks.)

9. Event displays tend to be clean and contain few clusters which are not associated with tracks from a common vertex. Fig. 16 shows a relatively high multiplicity but otherwise typical event.

10. The distribution of cluster hit multiplicity in one typical detector is shown as the solid line in Fig. 17(a). The points on this figure are from a Monte Carlo simulation[3]. The Monte Carlo points were normalized to have the same number of events with at least one hit as the data. Apart from an excess of events with no hits, the data and Monte Carlo are seen to agree rather well. The average hit multiplicity per detector of the real data is 1.8. The distribution of hits as a function of strip number is shown in Fig. 17(b). Data is shown as a solid curve and the results of the Monte Carlo simulation are shown as points. The Monte Carlo data has been normalized to have the same number of hits as the data in the right-most bin. Again, agreement between data and Monte Carlo is good. This agreement encourages the conclusion that Monte Carlo event generator describes the data reasonably well and that almost all hit clusters are caused by event-associated charged particles.

11. Fig. 18 shows further evidence for the lack of background from sources unrelated to events. In both parts of this figure, we plot the average cluster width as a function of track slope for events with found vertices. In part (a), only clusters which are on found tracks are used while in part (b), clusters which are not associated with the found tracks are used. The "slope" for a cluster in part (b) is computed from the line joining the cluster center to the found vertex point. The fact that the lines in (a) and (b) are nearly the same indicates that clusters not associated with found tracks are nonetheless event-related (such clusters come mainly from particles which traverse fewer than three planes).

12. Finally, Fig. 19 shows the vertical projection of found vertex points using tracks from the lower half-detector only. The r.m.s. width of this distribution ($\sigma = 105\mu$m) is compatible with the beam width.

# 7 Conclusions

A large silicon system was assembled and operated at very short distance from the Sp$\bar{p}$S-collider beam, in the LSS5 high luminosity interaction region.

The detector performance was satisfactory with signal to noise ratios in the range 20 to 30, which allows an on-line pedestal subtraction and zero suppression with high efficiency.

The background due to beam halo particles, and the effect of RF induced signal from bunch crossing was found to be negligible.

The success of this test leads to the conclusion that a detector of this kind might be very effective in tagging beauty particles produced in the forward region in high energy hadronic collider, at the level of both on-line trigger and off-line analysis.

# References

[1] Proposal P238, Study of Beauty Physics at the SPS-Collider with Real-Time Use of Silicon Microvertex Information, CERN-SPSC/88-33;
P238Add.1, Measurement of $B_s$ Mixing, CERN-SPSC/89-43;
P238Add.2, Request For Collider Test of Silicon Microvertex Detector, CERN-SPSC/89-55;

[3] Events were generated using Isajet and the Sp$\bar{p}$S vertex distribution. Detector hits were generated by projecting charged particle momentum vectors to a detector plane position. A more detailed Monte Carlo simulation is in progress.

P238Add.3, Further Comments on Collider Test of Silicon Microvertex Detector, CERN-SPSC/89-61.

[2] M. Caccia et al., NIM A260 (87)124.

[3] S.A. Kleinfelder et al., IEEE Trans. Nucl. Sci. 35 (1989) 171.

[4] F. Kirsten and C. Haber, IEEE Trans. Nucl. Sci. 37 (1990) 288.

[5] A. Lang and J.P. Vanuxem.

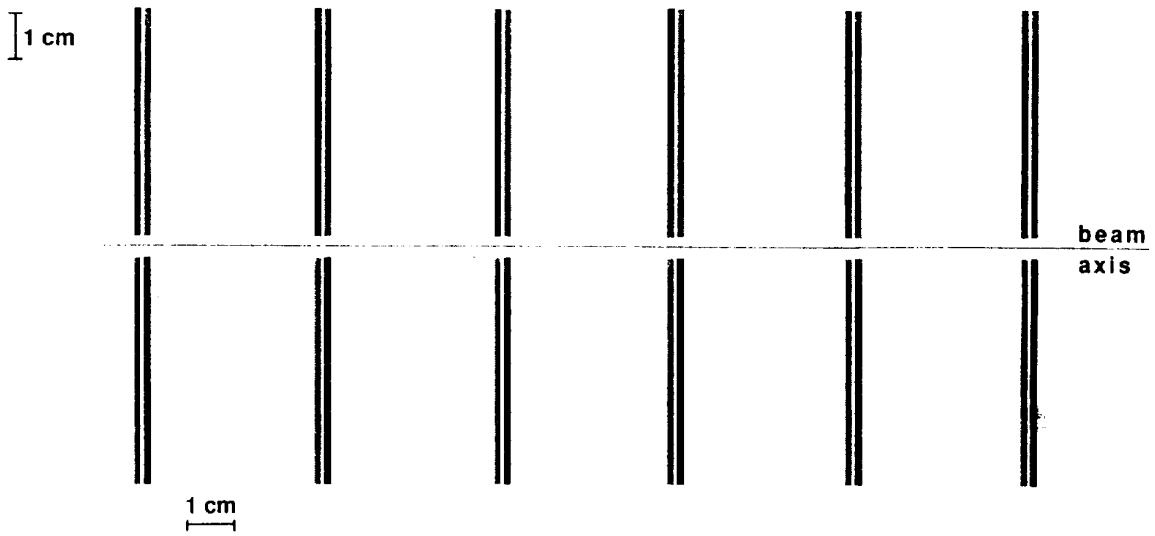


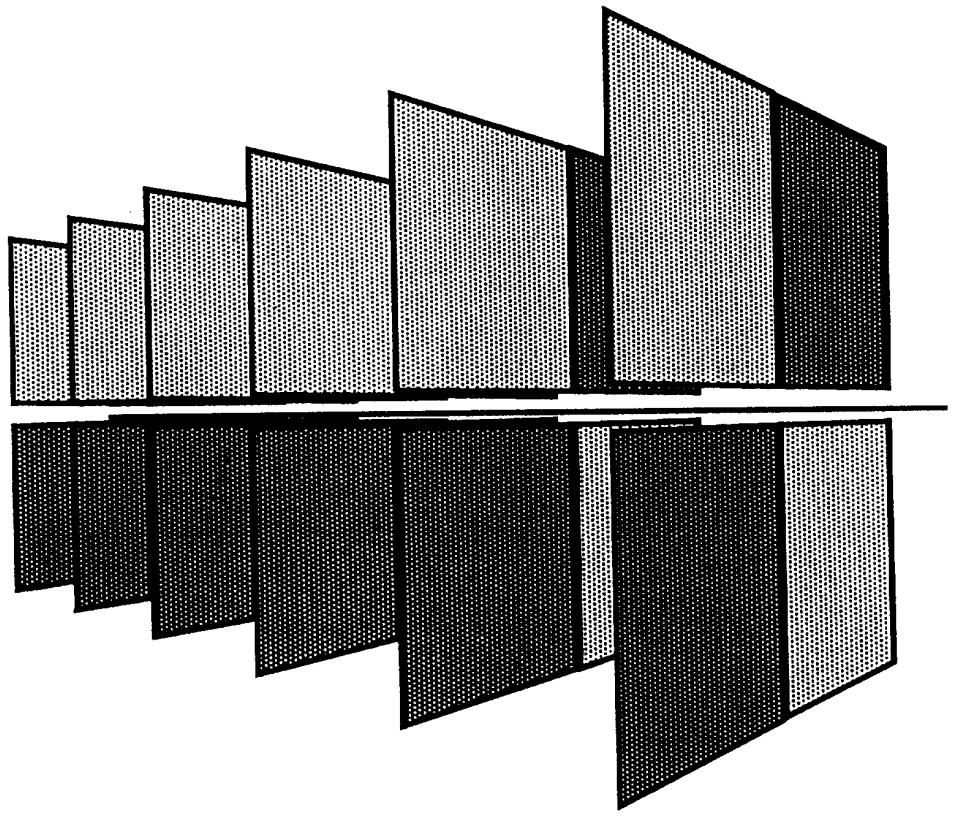

Figure 1: (a) Side view of the detector configuration. The black lines indicate the x-view detector positions and the gray lines indicate the y-view detector positions. (b) Perspective drawing of detector. Only four of the eight detectors in each plane are visible. The strip orientation of the hidden detectors is perpendicular to that of the detectors they face.

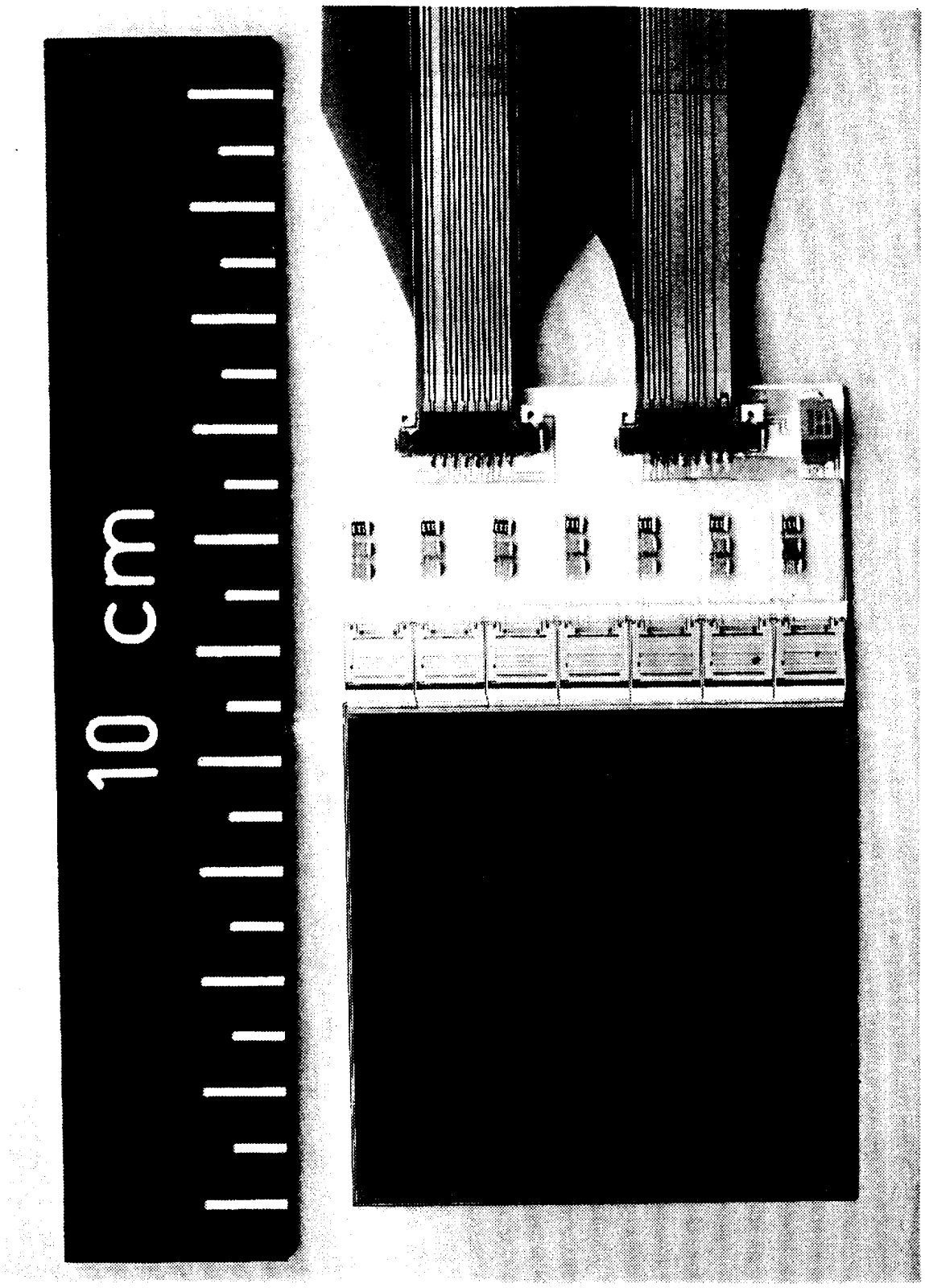


Figure 2: Photograph of a single silicon strip detector with its associated alumina hybrid and readout chips.

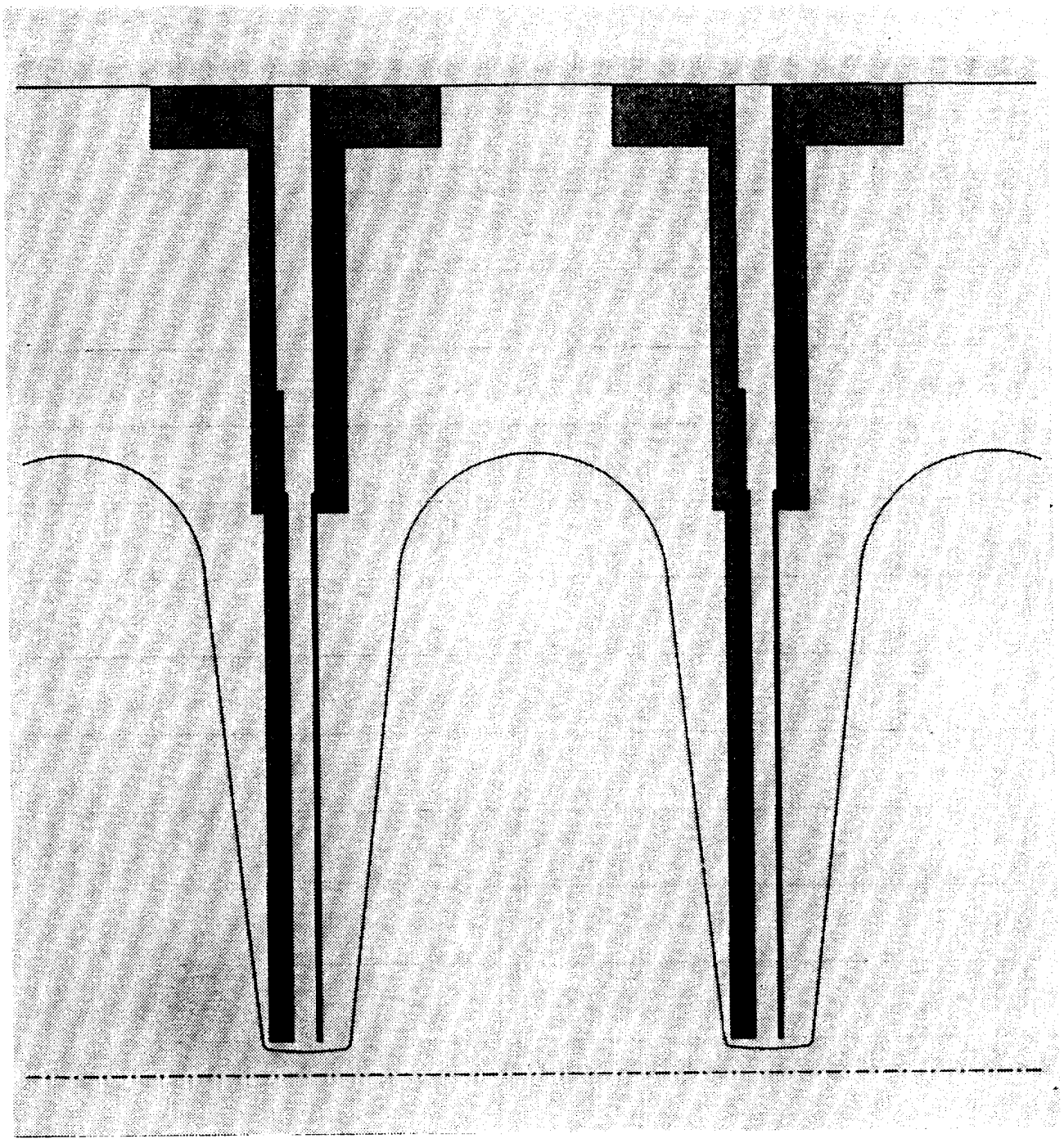

Figure 3: Side view showing two detector planes. The y-view detectors for each plane are on the left of the corresponding x-view detectors.

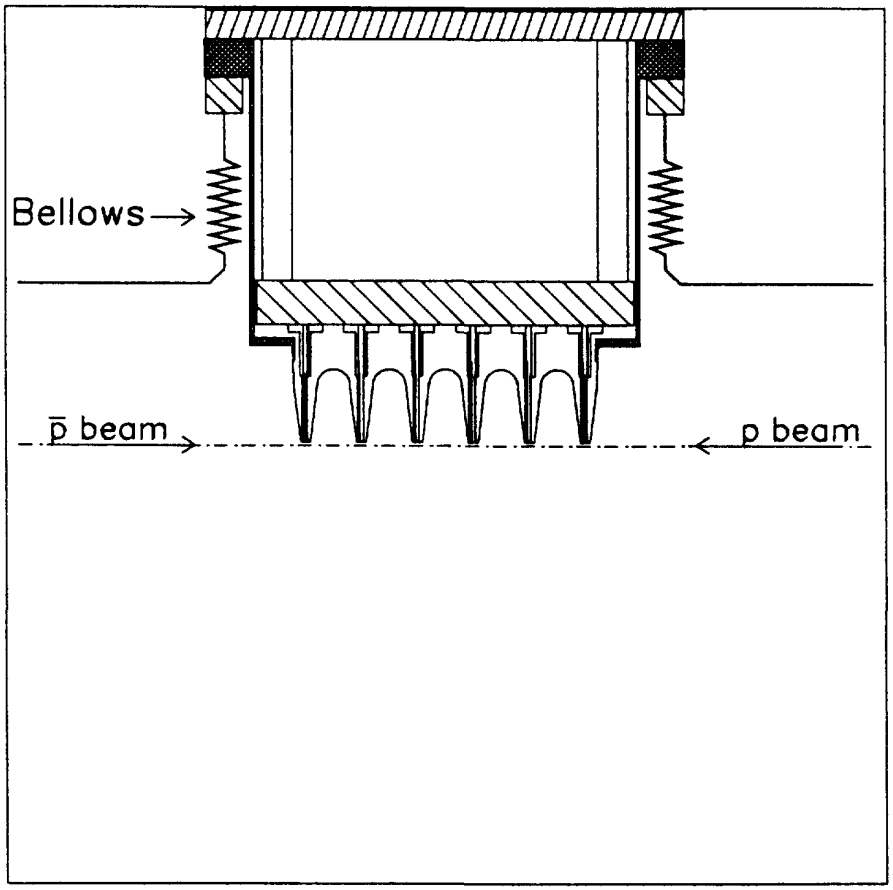


Figure 4: Sketch of the upper silicon half-detector mounted inside a Roman Pot. The bottom of the corrugated window is shown at a distance of 1.5 mm from the beam.

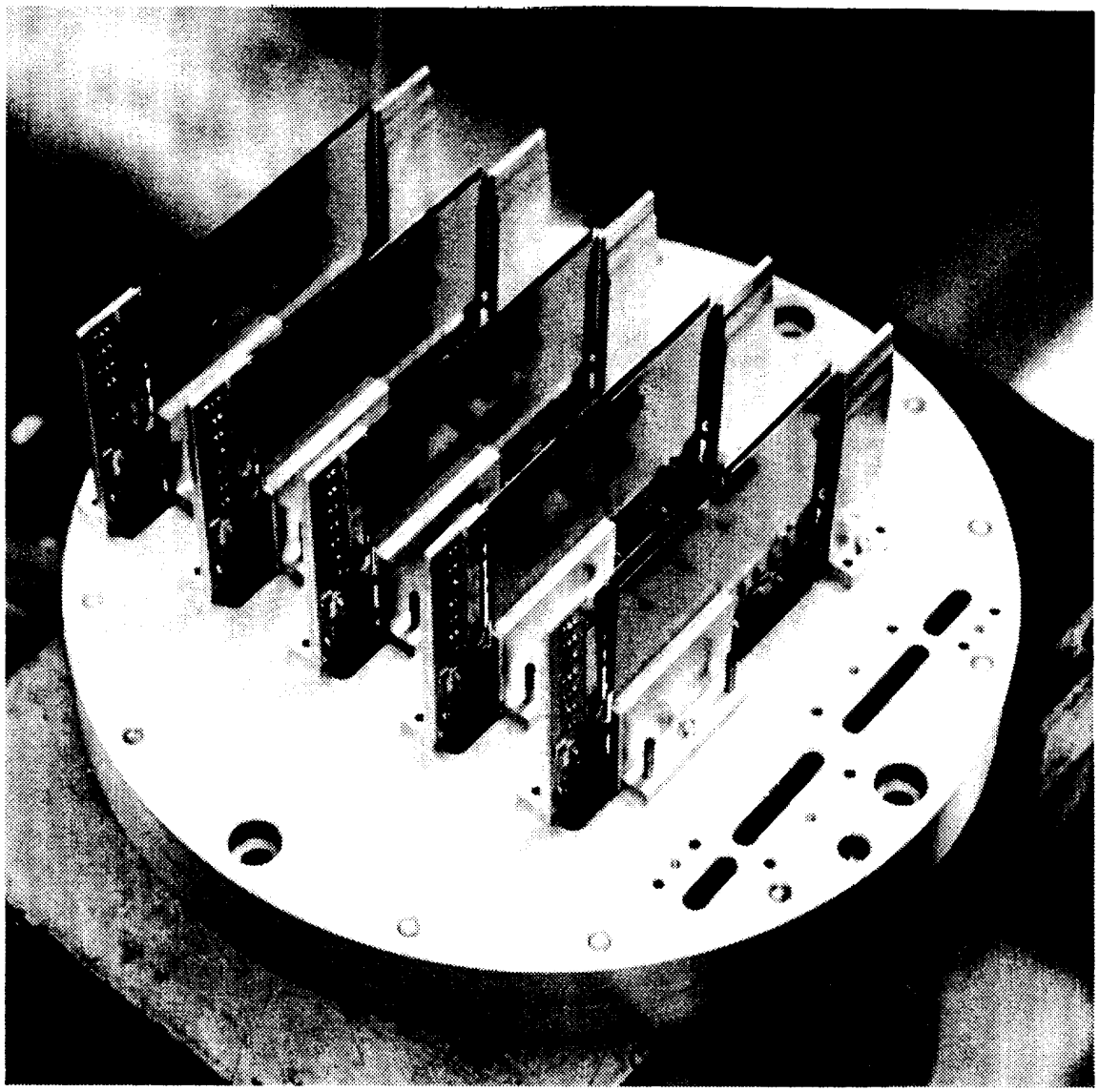

Figure 5: Photograph of a partially assembled half-detector. Five of the six planes had been mounted at the time the photograph was taken.

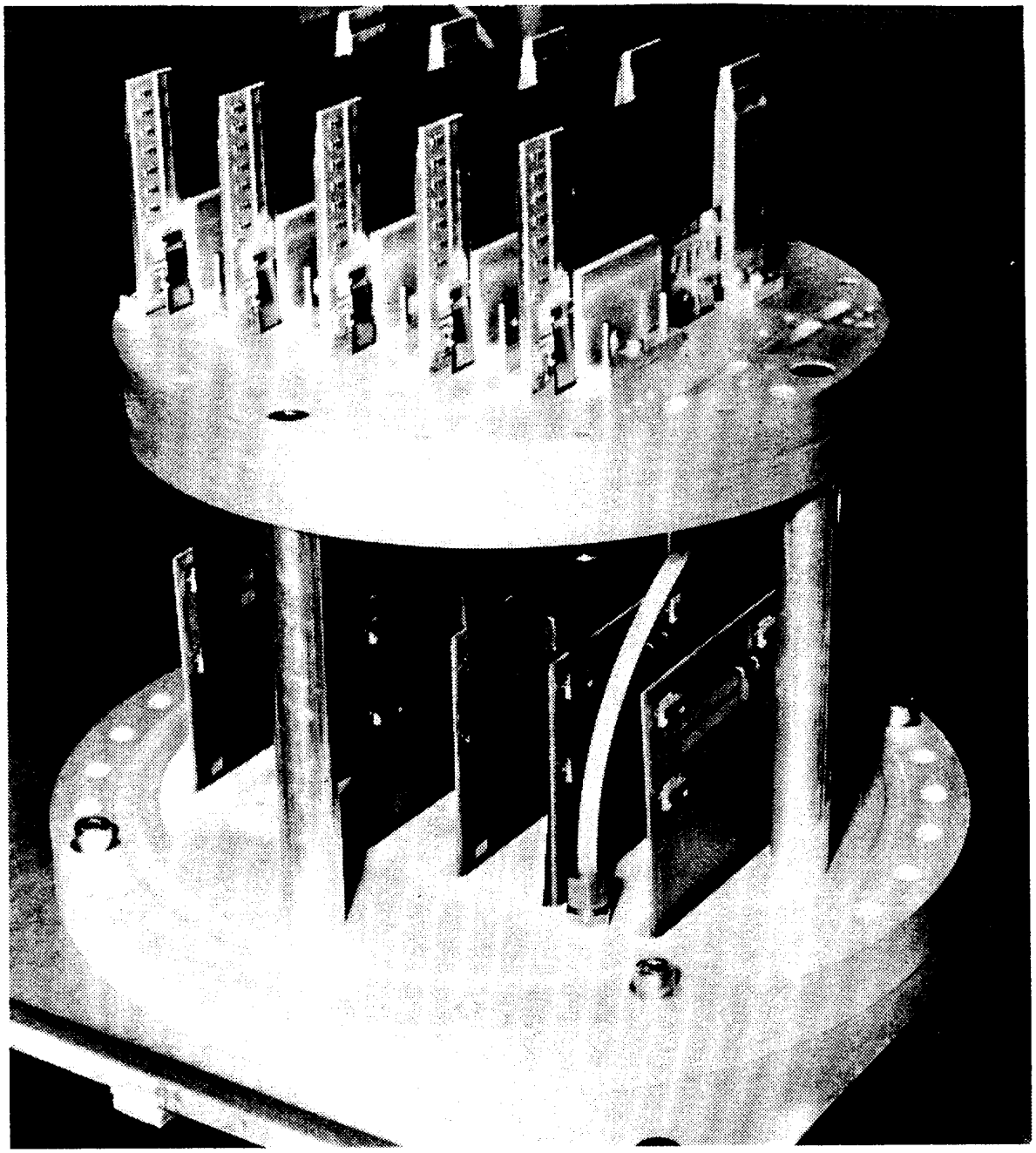

Figure 6: Photograph of the five-plane assembly joined to a vacuum bulkhead.

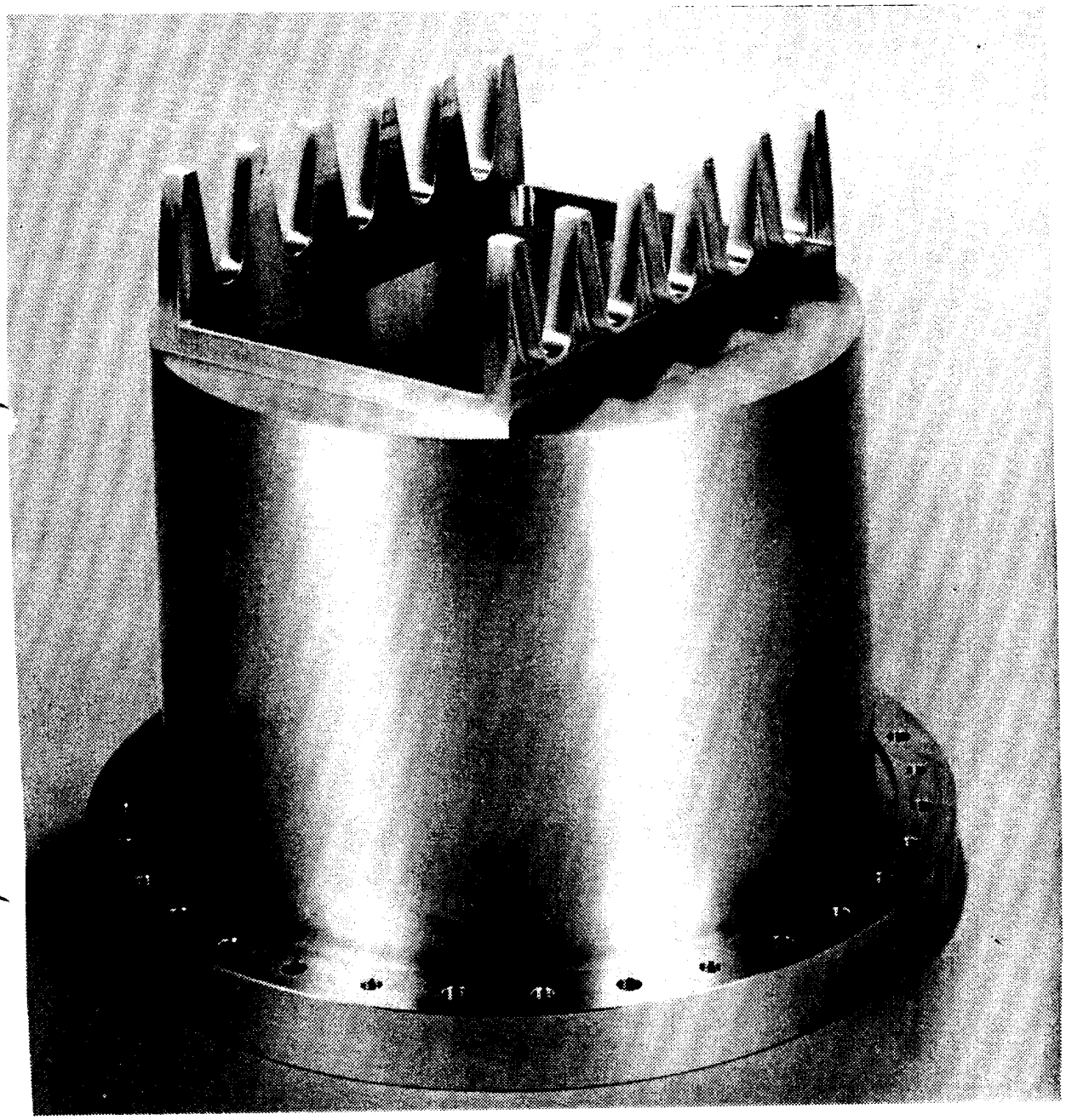

Figure 7: Photograph of a Roman Pot, taken before mounting of the corrugated window.

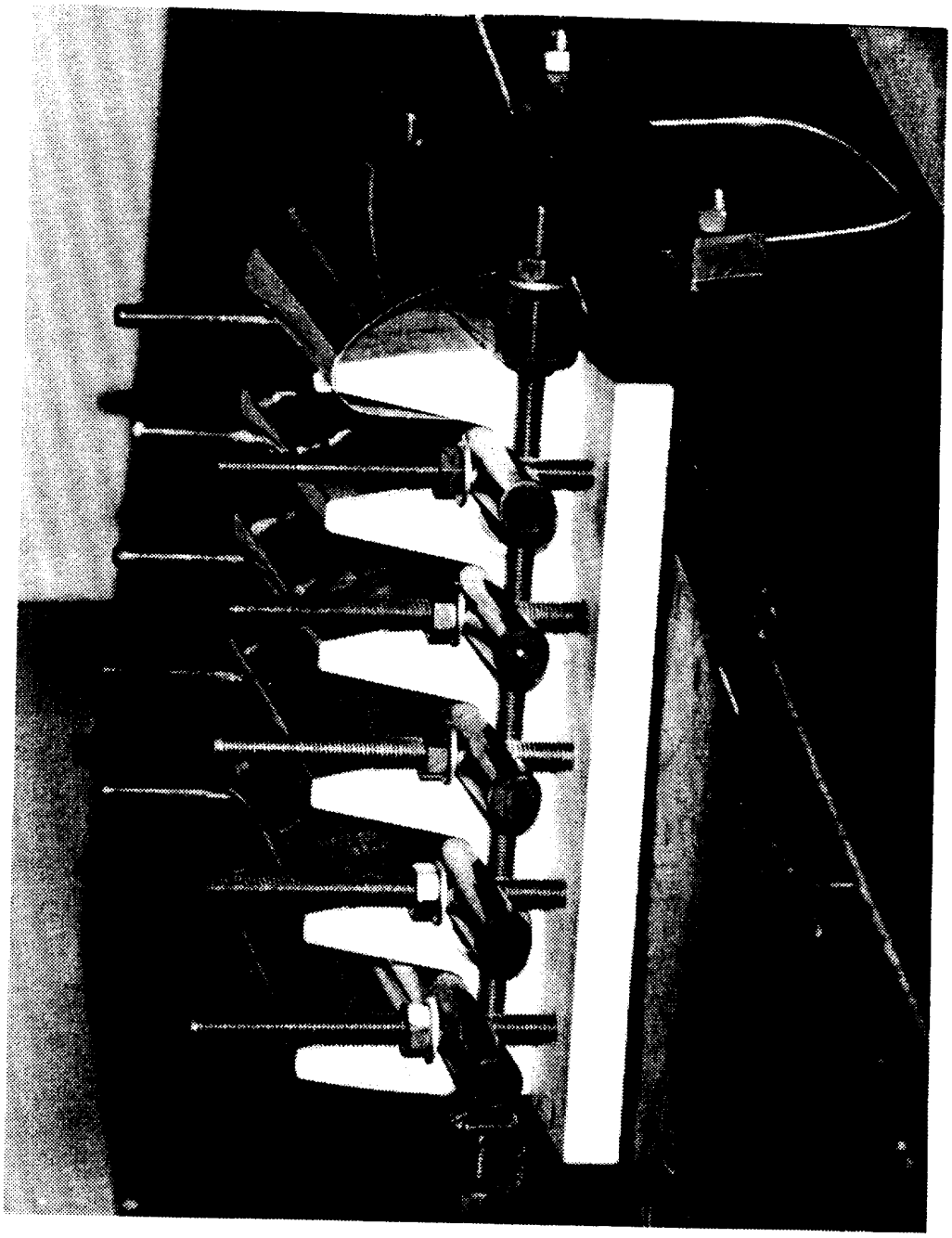

Figure 8: Jig used for pre-forming the 200 $\mu$m aluminum window.

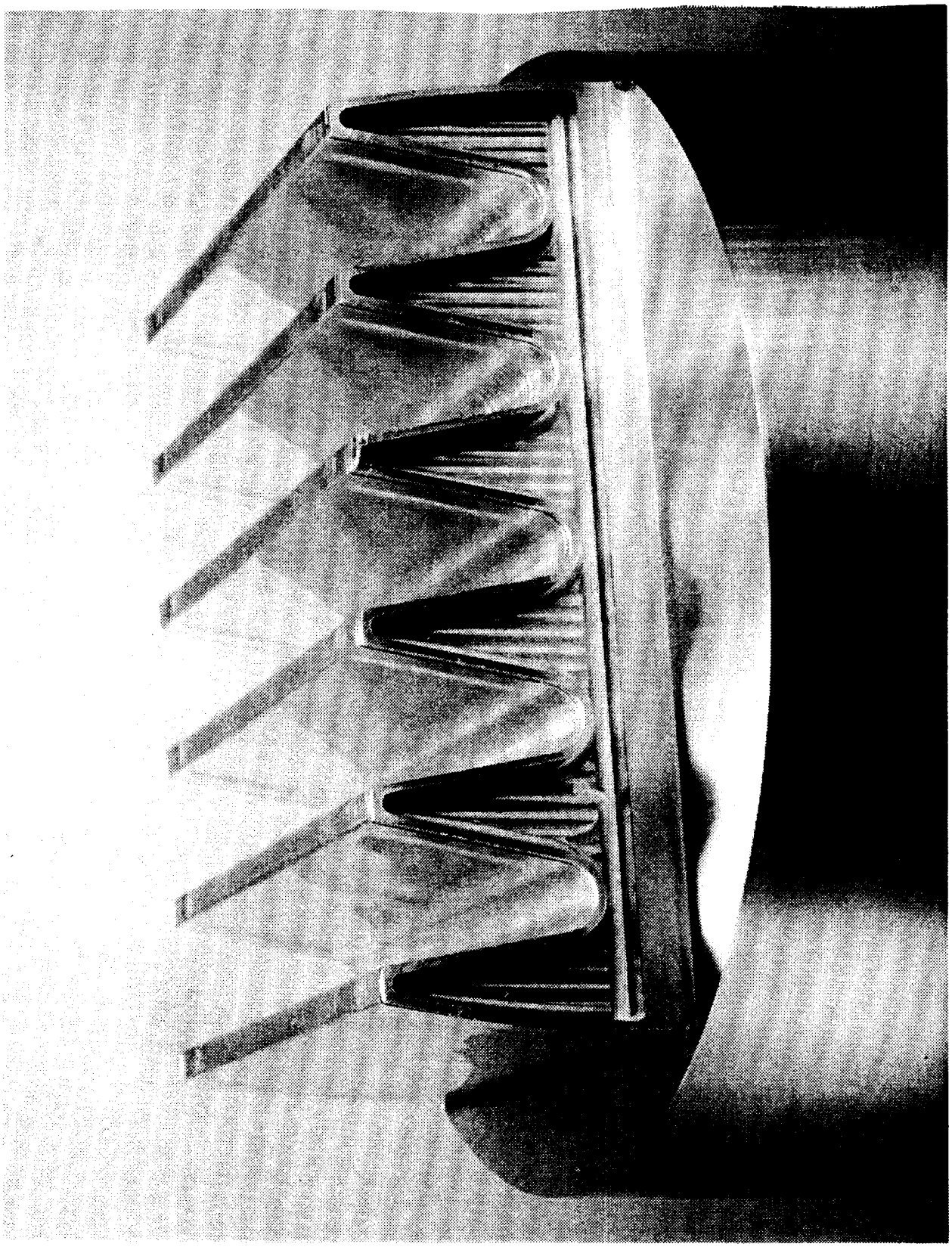

Figure 9: Close up photograph of the corrugated window on the Roman Pot designed for this test.

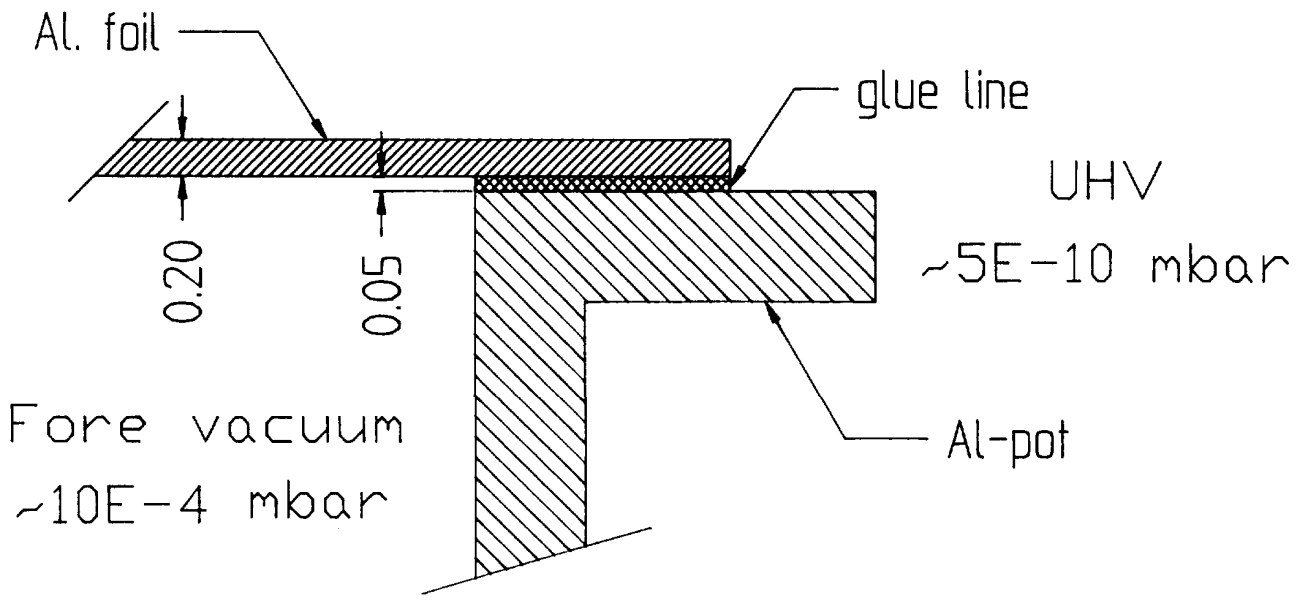


Figure 10: Detail of the joint between the 200 $\mu$m window and the Roman Pot.

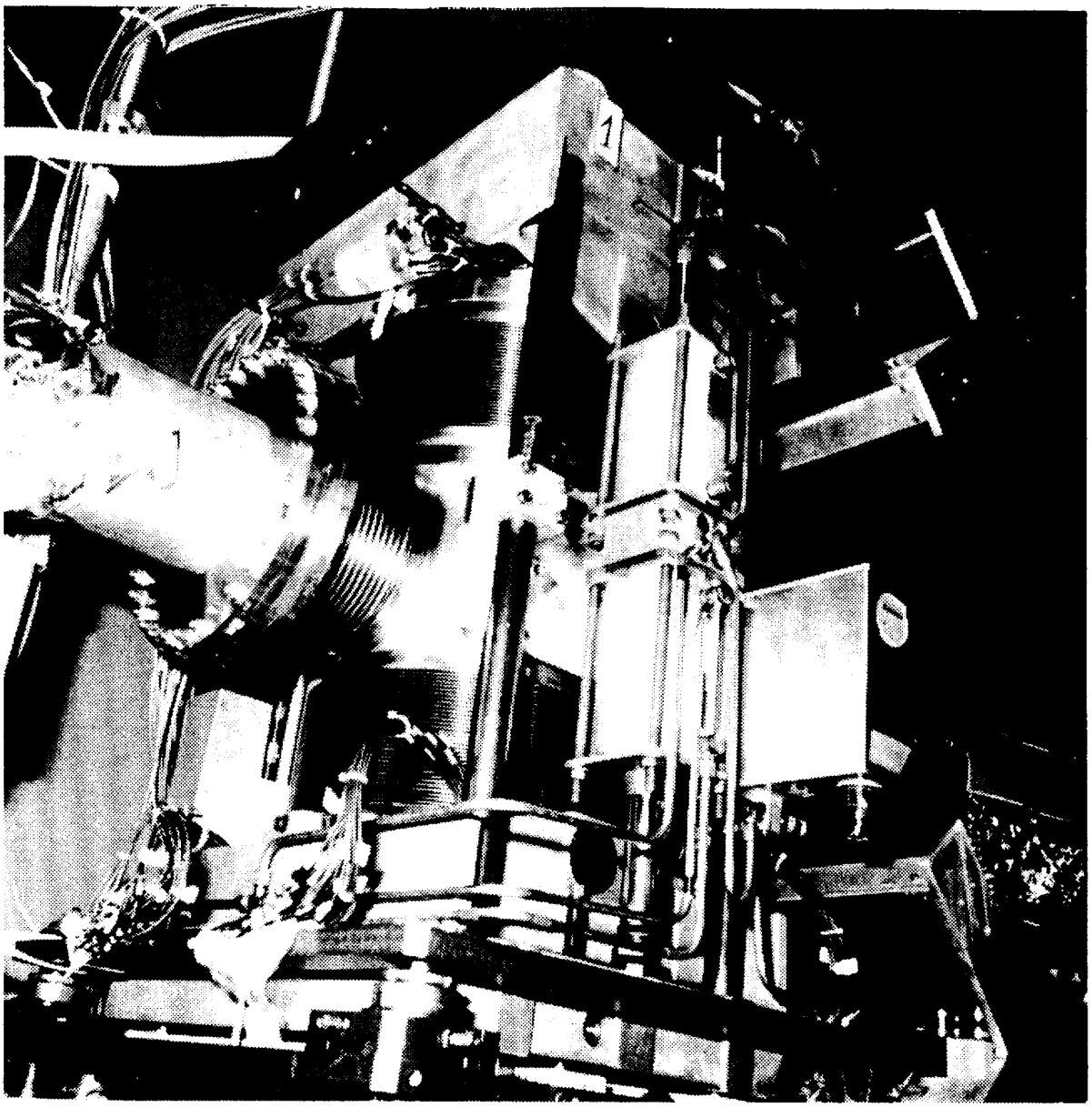

Figure 11: Pot positioning mechanism, after installation in LSS5.

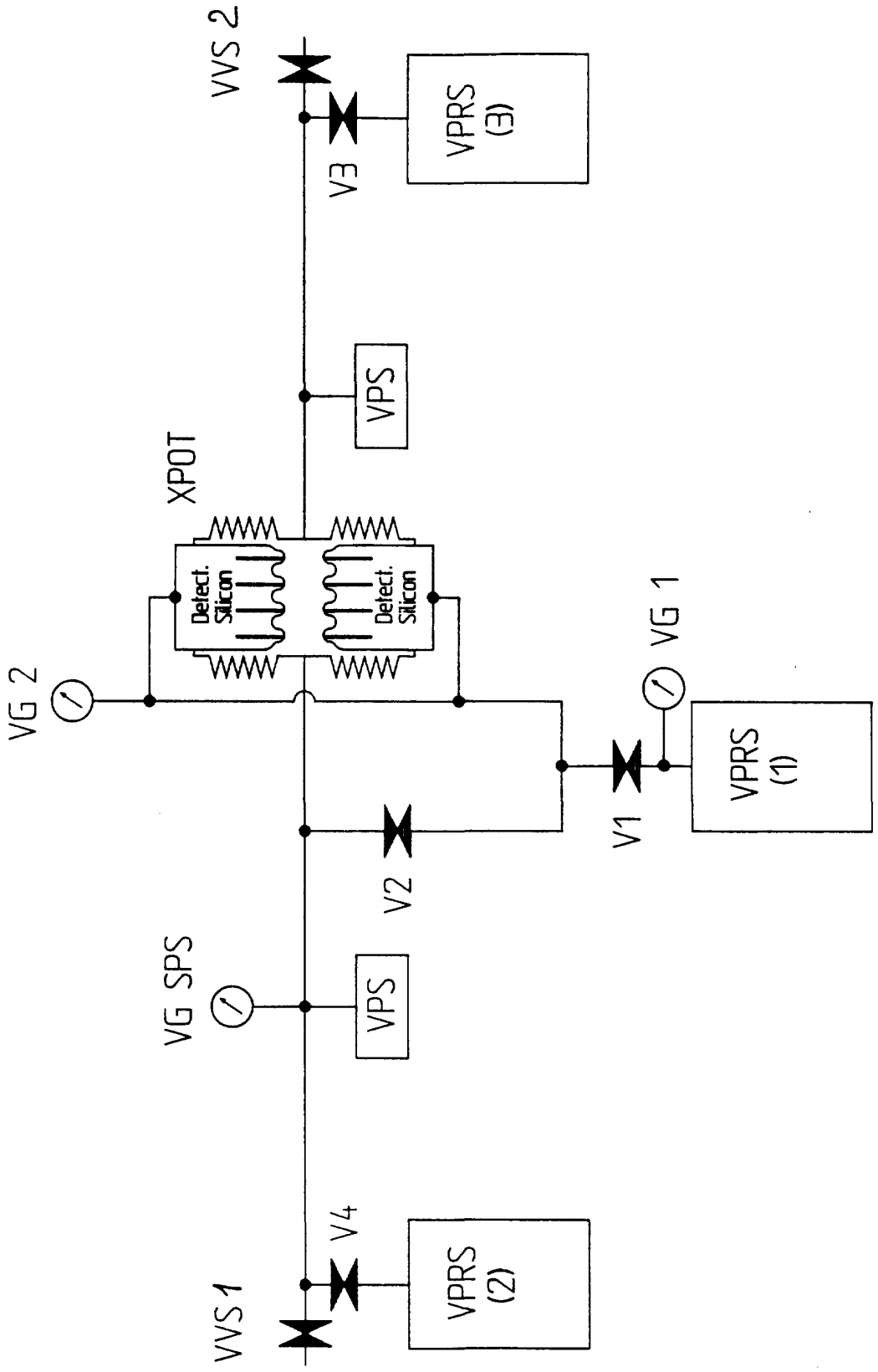


Figure 12: Schematic layout of the vacuum pumping system.

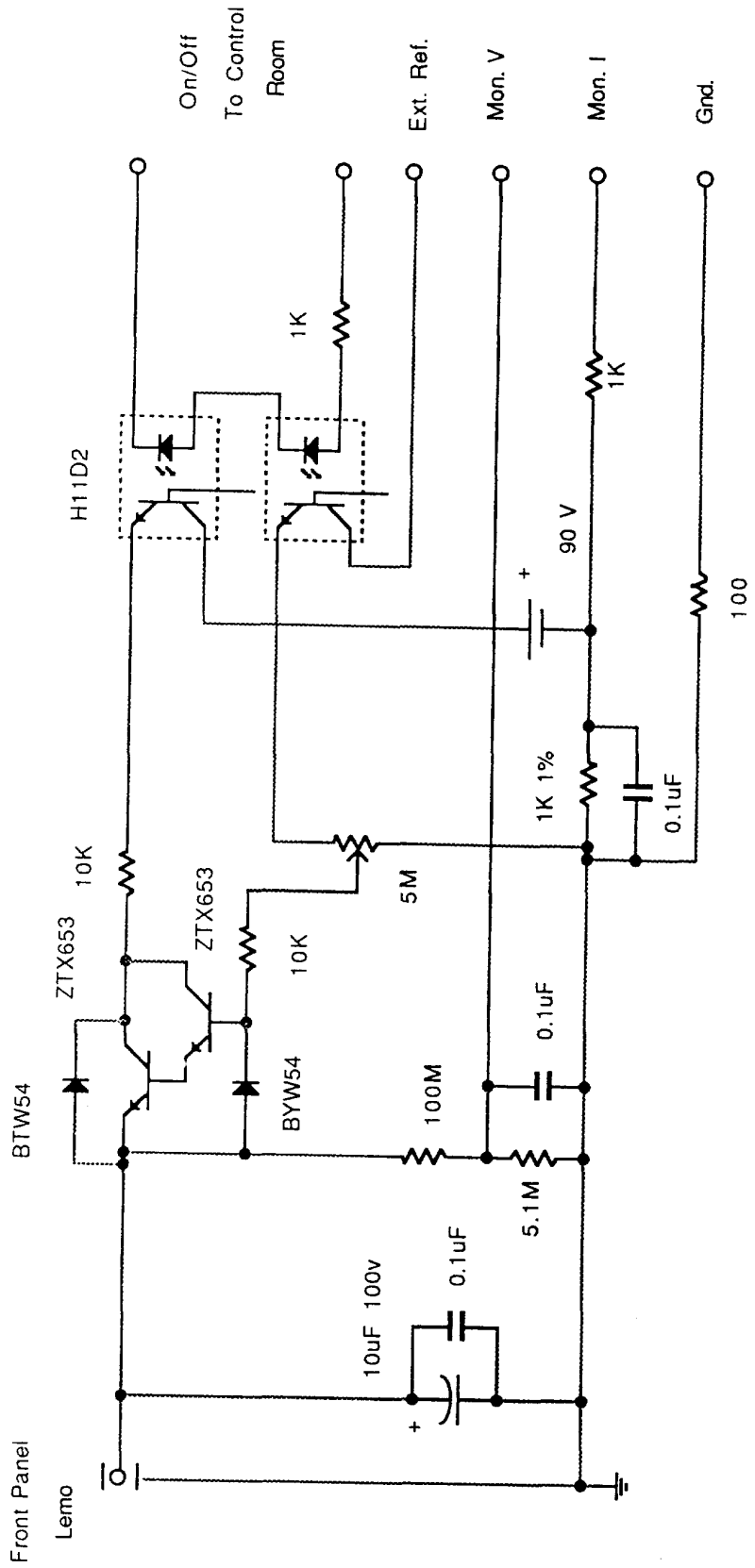


Figure 13: Power supply bias and control circuit.

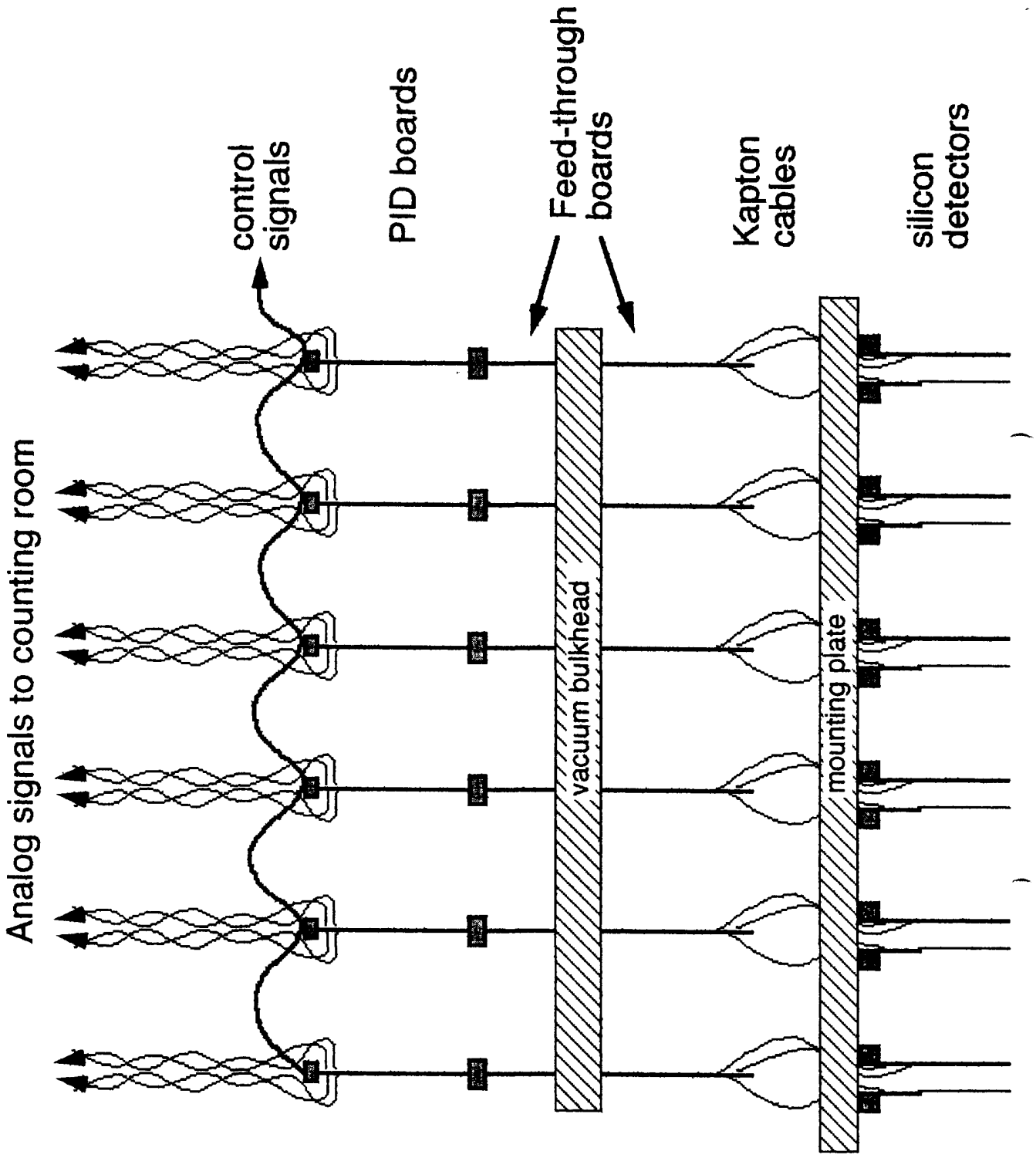


Figure 14: Schematic of readout and control pathes for one detector hodoscope.

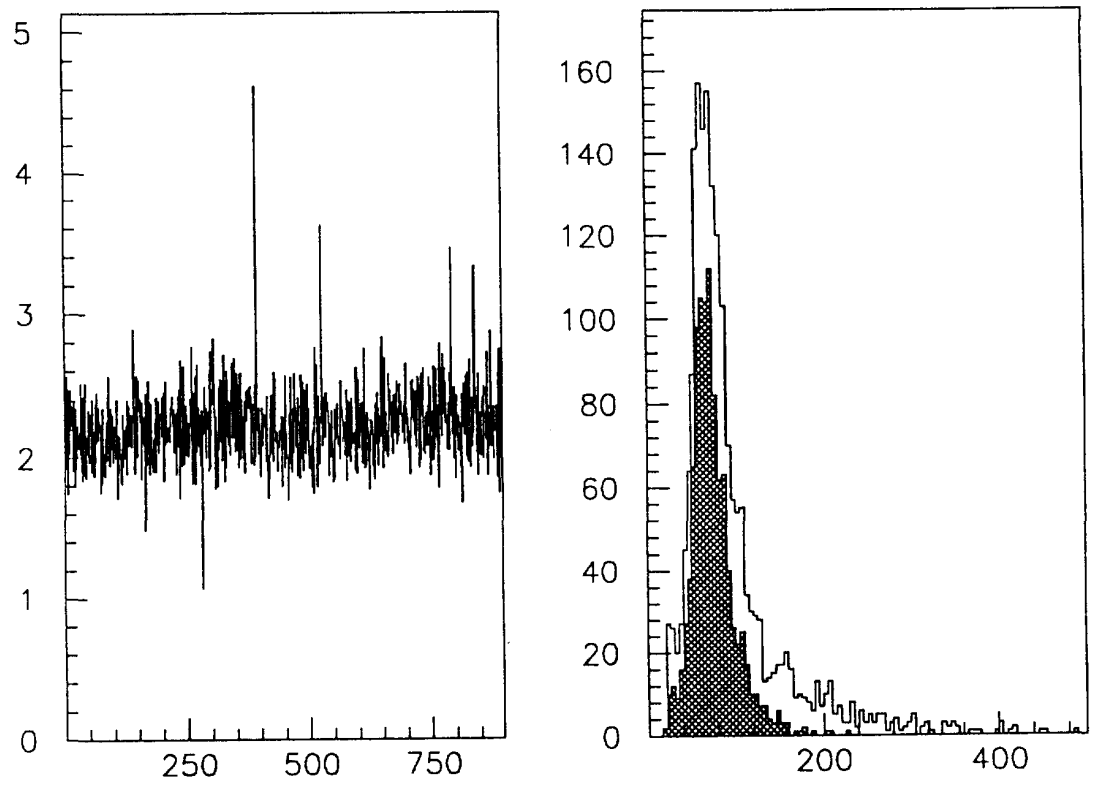


Figure 15: (a) The rms noise of a typical detector plotted vs. channel number. (b) Cluster pulse height distributions. The unhatched histogram is for all clusters with width less than four strips. The hatched histogram is for all width=2 clusters.

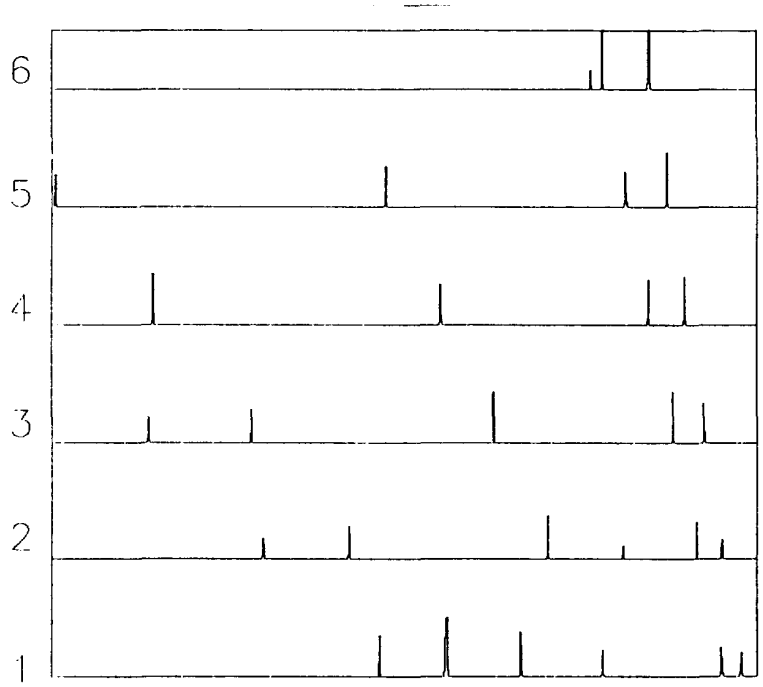


Figure 16: Pulse height distribution vs.channel for the six planes of one detector quadrant for a single event. Only pulse heights greater than 4 times the rms noise are plotted.

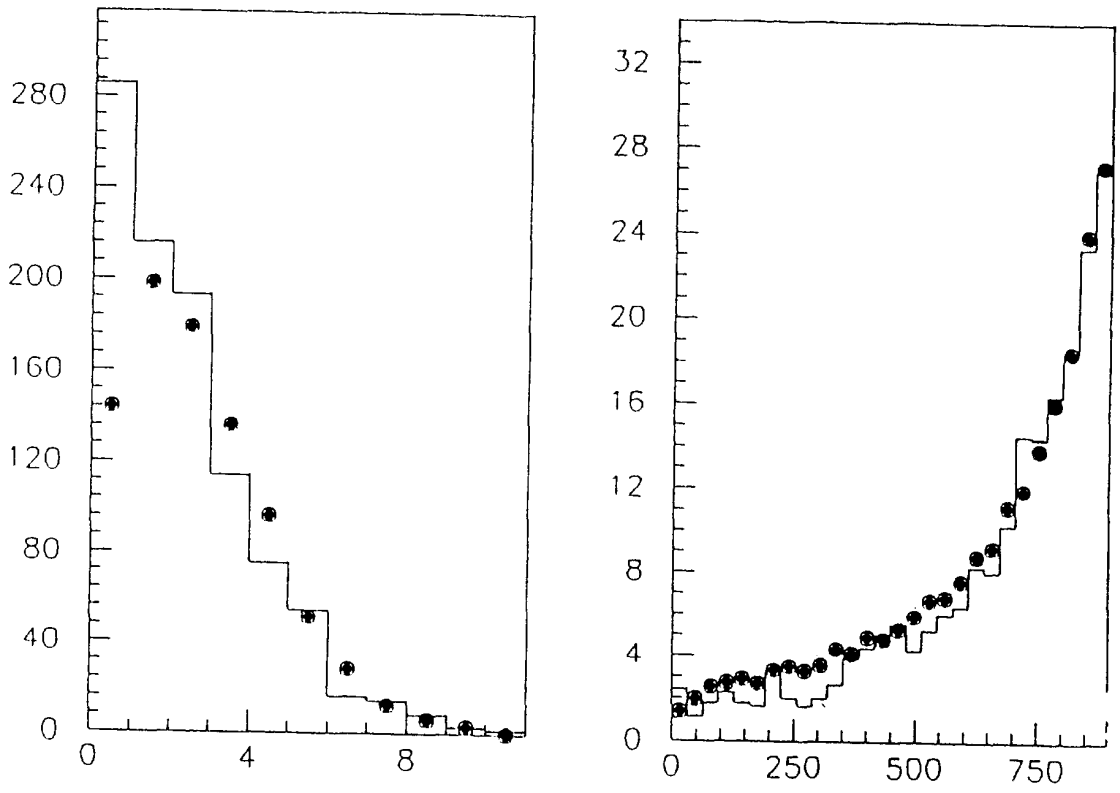


Figure 17: (a) Hit multiplicity distribution on one detector. The average hit multiplicity is 1.8. (b) Hit distribution vs. channel number for a typical detector. In both (a) and (b), the solid line indicates the real data and the points are the result of a Monte Carlo simulation which is described in the text.

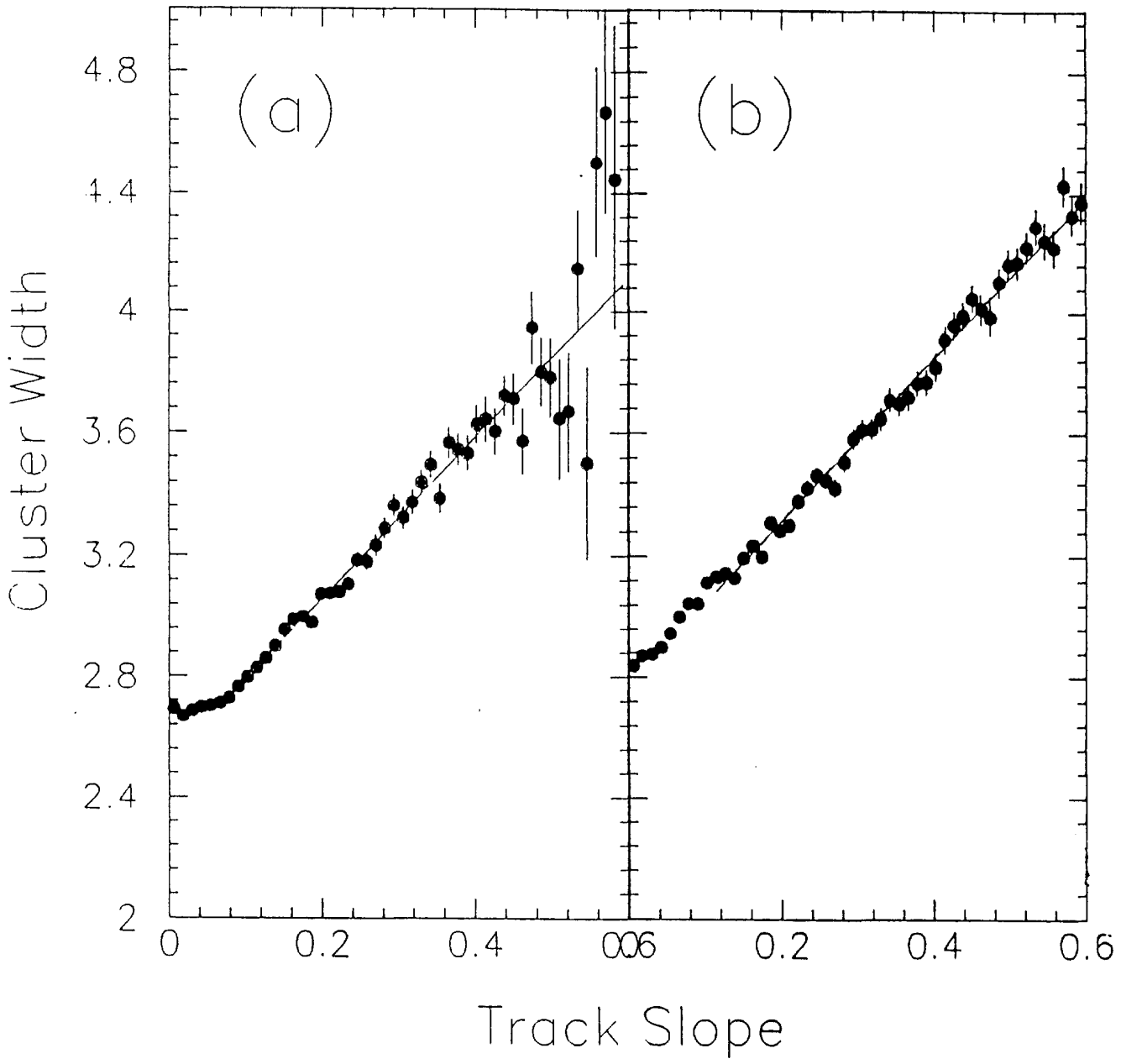


Figure 18: The average cluster width as a function of track slope for events with found vertices. In part (a), only clusters from found tracks are used while in part (b), clusters which are not associated with found tracks are used.

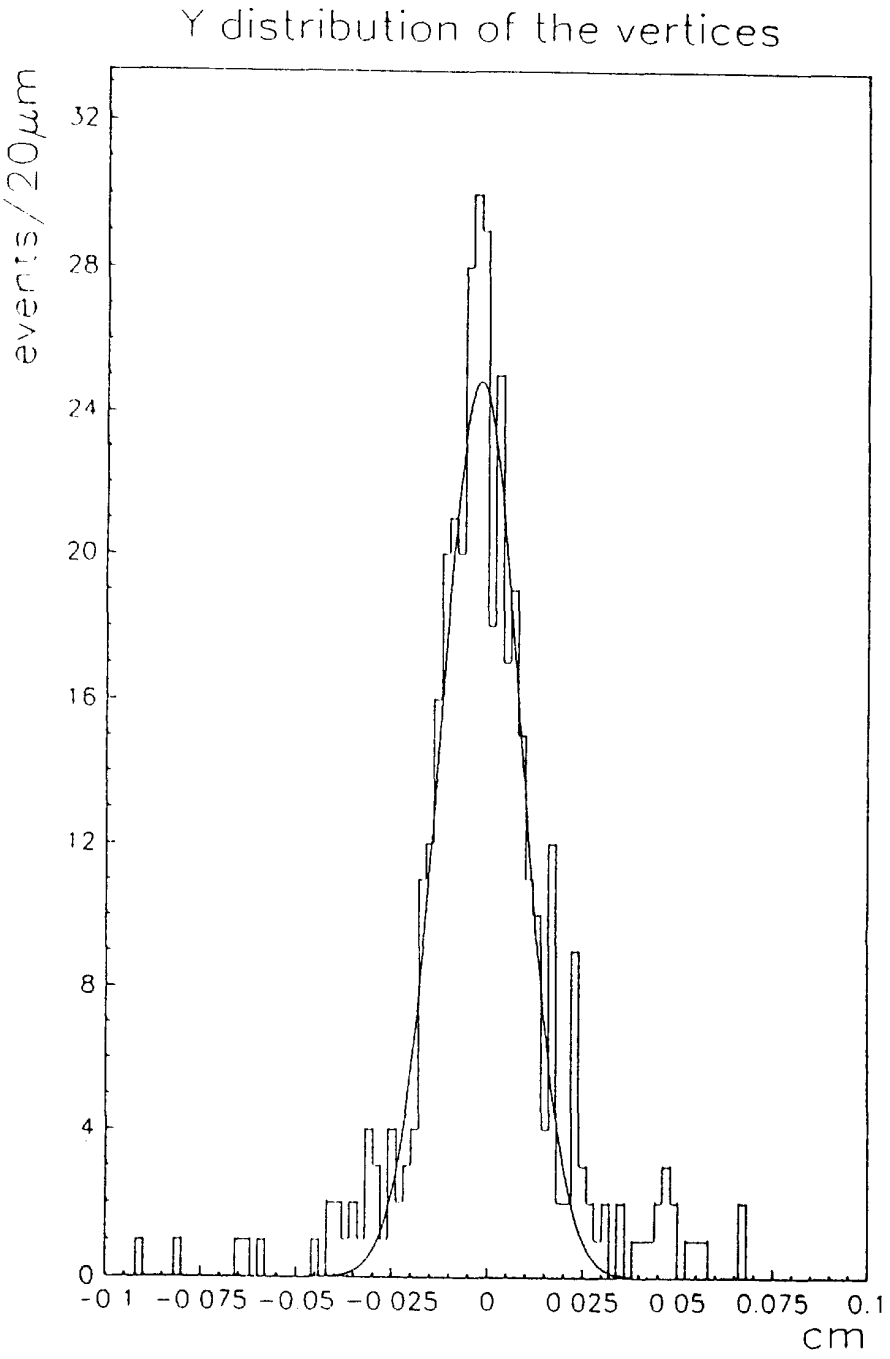


Figure 19: The vertical projection of found vertex points using tracks from the lower half-detector only, in the interval (+12cm,+8cm) along the beam direction. The r.m.s. width of this distribution ($\sigma = 105\mu$m) is compatible with the beam width.